Publications of the Astronomical Society of Australia (PASA), Vol. 33, e055, 29 pages (2016).

doi:10.1017/pasa.2016.47

The ANU WiFeS SuperNovA Programme (AWSNAP)

Michael J. Childress[1,2,3,12], Brad E. Tucker[1,2], Fang Yuan[1,2], Richard Scalzo[1], Ashley Ruiter[1,2], Ivo Seitenzahl[1,2], Bonnie Zhang[1], Brian Schmidt[1], Borja Anguiano[4], Suryashree Aniyan[1], Daniel D. R. Bayliss[1,5], Joao Bento[1], Michael Bessell[1], Fuyan Bian[1], Rebecca Davies[1], Michael Dopita[1], Lisa Fogarty[6], Amelia Fraser-McKelvie[7,8], Ken Freeman[1], Rajika Kuruwita[1], Anne M. Medling[1], Simon J. Murphy[1], Simon J. Murphy[6,9], Matthew Owers[4,10], Fiona Panther[1,2], Sarah M. Sweet[1], Adam D. Thomas[1] and George Zhou[11,1]

[1]Research School of Astronomy and Astrophysics, Australian National University, Canberra, ACT 2611, Australia
[2]ARC Centre of Excellence for All-sky Astrophysics (CAASTRO), Canberra, ACT, Australia
[3]School of Physics and Astronomy, University of Southampton, Southampton, SO17 1BJ, UK
[4]Department of Physics and Astronomy, Macquarie University, NSW 2109, Australia
[5]Observatoire Astronomique de l'Université de Genève, 51 ch. des Maillettes, 1290 Versoix, Switzerland
[6]Sydney Institute for Astronomy (SIfA), School of Physics, The University of Sydney, NSW 2006, Australia
[7]School of Physics and Astronomy, Monash University, Clayton, Victoria 3800, Australia
[8]Monash Centre for Astrophysics (MoCA), Monash University, Clayton, Victoria 3800, Australia
[9]Stellar Astrophysics Centre, Department of Physics and Astronomy, Aarhus University, 8000 Aarhus C, Denmark
[10]Australian Astronomical Observatory, PO Box 915, North Ryde, NSW 1670, Australia
[11]Harvard-Smithsonian Center for Astrophysics, 60 Garden St, Cambridge, MA 02138, USA
[12]Email: m.j.childress@soton.ac.uk

(Received July 11, 2016; Accepted October 5, 2016)

Abstract

This paper presents the first major data release and survey description for the ANU WiFeS SuperNovA Programme. ANU WiFeS SuperNovA Programme is an ongoing supernova spectroscopy campaign utilising the Wide Field Spectrograph on the Australian National University 2.3-m telescope. The first and primary data release of this programme (AWSNAP-DR1) releases 357 spectra of 175 unique objects collected over 82 equivalent full nights of observing from 2012 July to 2015 August. These spectra have been made publicly available via the WISEREP supernova spectroscopy repository.

We analyse the ANU WiFeS SuperNovA Programme sample of Type Ia supernova spectra, including measurements of narrow sodium absorption features afforded by the high spectral resolution of the Wide Field Spectrograph instrument. In some cases, we were able to use the integral-field nature of the Wide Field Spectrograph instrument to measure the rotation velocity of the SN host galaxy near the SN location in order to obtain precision sodium absorption velocities. We also present an extensive time series of SN 2012dn, including a near-nebular spectrum which both confirms its 'super-Chandrasekhar' status and enables measurement of the sub-solar host metallicity at the SN site.

Keywords: supernovae: general – supernovae: individual: (SN 2012dn)

1 INTRODUCTION

In the last decade, wide-field extragalactic transient surveys—such as the Palomar Transient Factory (PTF; Rau et al. 2009; Law et al. 2009), the Panoramic Survey Telescope and Rapid Response System (PanSTARRS; Kaiser et al. 2010), the Catalina Real-time Transient Survey (CRTS; Drake et al. 2009), the Texas Supernova Search (Quimby 2006; Yuan 2010), and the All-Sky Automated Survey for Supernovae (ASAS-SN; Shappee et al. 2014; Holoien et al. 2016)—have revolutionised our understanding of the myriad ways in which stars explode through the discovery of new classes of exotic transients. Simultaneously, these surveys have discovered hundreds of supernovae (SNe) of 'traditional' types (see Filippenko 1997, for a review), enabling statistical analyses of the properties of these SNe.

Whilst imaging surveys have provided discovery and light curves for this wealth of new transients, complementary spectroscopy surveys have provided the critical insight into the physical origins of these events. Numerous supernova spectroscopy surveys have released thousands of high-quality spectra of nearby SNe into the public domain (Matheson et al. 2008; Blondin et al. 2012; Silverman et al. 2012c; Folatelli et al. 2013; Modjaz et al. 2014). These surveys have frequently been dedicated to the spectroscopic follow-up of

Type Ia supernovae (SNe Ia) which, due to their rates and luminosities, dominate any magnitude-limited imaging survey. Such surveys have revealed that photometrically similar SNe can still exhibit diversity of spectroscopic behaviour, indicating spectra remain a critical tool for revealing the full nature of the supernova progenitors (particularly for SNe Ia). Additionally, spectra remain critical for supernova classification—particularly at early phases when the full photometric evolution has yet to be revealed. Such early classifications then inform the use of additional SN follow-up facilities, including those operating outside the optical window.

Recently, the Public ESO Spectroscopic Survey for Transient Objects (PESSTO; Smartt et al. 2015) began a multi-year programme on the NTT 3.6-m telescope in Chile, with the goal of obtaining high-quality spectral time series for roughly 100 transients (of all kinds) to be released to the public. This survey has already released hundreds of spectra in its first two annual data releases, and continues to release all SN classification spectra within typically 1 d from observation. Other ongoing SN spectroscopy programmes, such as the Asiago Supernova Programme (Tomasella et al. 2014), also make important contributions to the transient community through timely SN classification and spectroscopy releases.

Here, we describe our ongoing spectroscopy programme AWSNAP—the **A**NU **W**iFeS **S**uper**N**ov**A** **P**rogramme—which uses the Wide Field Spectrograph (WiFeS; Dopita et al. 2007, 2010) on the Australian National University (ANU) 2.3-m telescope at Siding Spring Observatory in Australia. In this paper, we describe the data processing procedures for this ongoing programme, and describe the first AWSNAP data release (AWSNAP DR1) comprising 357 spectra of 175 supernova of various types obtained during 82 classically scheduled observing nights over a 3-yr period from 2012 July to 2015 August. Most of these spectra have been released publicly via the Weizmann Interactive Supernova data REPository (WISeREP[1]— Yaron & Gal-Yam 2012), with the remainder set to be released within the next year as part of forthcoming PESSTO papers. This programme will continue to observe SNe of interest and classify SN discoveries from transient searches such as the new SkyMapper Transients Survey (Keller et al. 2007). We aim to release future SN classification spectra from AWSNAP publicly via WISeREP in parallel with any classification announcements.

This paper is organised as follows. Section 2 describes the WiFeS data processing and SN spectrum extraction procedures. Section 3 presents general properties of our SN sample and compares AWSNAP DR1 to other public SN spectra releases. In Section 4, we present some analysis of the properties of the SNe Ia in our sample, including measurement of narrow sodium absorption features afforded by the intermediate resolution of the WiFeS spectrograph. Some concluding remarks follow in Section 5.

[1] http://wiserep.weizmann.ac.il

Table 1. Details of WiFeS gratings.

Grating	λ_{min}	λ_{max}	Pixel size	Resolution
B3000	3 500 Å	5 700 Å	0.77 Å	1.5 Å
R3000	5 400 Å	9 570 Å	1.25 Å	2.5 Å
R7000	5 400 Å	7 020 Å	0.44 Å	0.9 Å

2 OBSERVATIONS AND DATA DESCRIPTION

Observations for AWSNAP were conducted with the WiFeS—(Dopita et al. 2007, 2010) on the ANU 2.3-m telescope at Siding Spring Observatory in northern New South Wales, Australia. Observing nights were classically scheduled with a single night of observing every 8–15 d. On some occasions, special objects of interest were observed during non-AWSNAP nights. A full list of the AWSNAP transient spectra is presented in Table A3 in Appendix A. In the sections that follow, we describe the processing of the WiFeS data, then characterise both the long-term performance of the WiFeS instrument and observing conditions at Siding Spring.

2.1. Data reduction and supernova spectrum extraction

The WiFeS instrument is an image-slicing integral field spectrograph with a wide 25 arcsec × 38 ″arcsec field of view. For AWSNAP, this frequently provided simultaneous integral field observations of SNe and their host galaxies. The WiFeS image slicer breaks the field of view into 25 'slitlets' of width 1 arcsec, which then pass through a dichroic beamsplitter and volume phase holographic (VPH) gratings before arriving at 4k × 4k CCD detectors. AWSNAP observations were always conducted with a CCD binning of 2 in the vertical direction—this sets the vertical spatial scale of the detector to be 1 arcsec, yielding final integral field elements (or 'spaxels') of size 1 arcsec × 1 arcsec. Typically seeing at Siding Spring is roughly 2 arcsec (see Section 2.3).

The VPH gratings utilised by WiFeS provide a higher wavelength resolution than traditional glass gratings. The low- and high-resolution gratings provide resolutions of $R = 3\,000$ and $R = 7\,000$, respectively, yielding velocity resolutions of up to $\sigma_v \sim 45$ km s^{-1} which is ideal for observing nebular emission lines from ionised regions in galaxies. For SNe, this can reveal narrow absorption features (see Section 4.2) from circumstellar material (CSM) which are typically smeared out by lower resolution spectrographs. AWSNAP observations were generally conducted with the lower resolution B3000 and R3000 gratings for the blue and red arms of the spectrograph, respectively, with the RT560 dichroic beamsplitter. Occasionally, the R7000 grating was deployed on the red arm to provide higher resolution observations of sodium absorption features. In Table 1, we provide the wavelength range, spectroscopic pixel size, and wavelength resolution (determined as the FWHM of calibration

lamp emission lines) for the three gratings used for AWSNAP observations.

Data for AWSNAP observations were reduced with version 0.7.0 of the PyWiFeS pipeline (Childress et al. 2014a). PyWiFeS performs standard image pre-processing such as overscan and bias subtraction, as well as cosmic ray rejection using a version of LACosmic (van Dokkum 2001) tailored for WiFeS data. The wavelength solution for WiFeS is derived using an optical model of the spectrograph which achieves an accuracy of 0.05 to 0.10Å (for $R = 7\,000$ and $R = 3\,000$, respectively) across the entire detector. Spectral flatfielding (i.e. correction of pixel-to-pixel quantum efficiency variations) is achieved with an internal quartz lamp, whilst spatial flat-fielding across the full instrument field of view is facilitated by twilight sky flats. Once the data has been pre-processed and flat-fielded, it is resampled onto a rectilinear three-dimensional (x, y, λ) grid (a 'data cube'). We then flux calibrate the data cubes with the use of spectrophotometric standard stars (from, e.g. Oke 1990; Bessell 1999; Stritzinger et al. 2005) and the Siding Spring Observatory extinction curve from Bessell (1999), whilst telluric features are removed using observations of smooth spectrum stars.

To further facilitate data reduction for the AWSNAP data release, we developed an SQL database for WiFeS observations using the Python Django framework. We created modified versions of the PyWiFeS reduction scripts that allow the user to request that all data from a specific night using a specific grating be fully reduced. The reduction scripts then query the database for all science observations and calibration data from that night and perform the required reduction procedures. For nights where a full suite of calibrations was not available (e.g. due to guest observations on a non-AWSNAP night), calibration solutions from the closest (in time) AWSNAP night were automatically identified via the database and employed in the reduction. Both the wavelength solution and spatial flat-fielding of the instrument are incredibly stable on long (∼year) timescales (see Section 2.2), thus validating the choice to use calibrations from different nights where necessary. This new database-driven data processing mode for PyWiFeS will be an important component of the upcoming effort to develop fully robotic queue-based observing capabilities for the ANU 2.3-m telescope.

The output of the PyWiFeS pipeline is a flux calibrated data cube that contains signal from the target supernova, the night sky, and occasionally the SN host galaxy. Extraction of the SN spectrum requires isolation of the spaxels containing supernova signal and subtraction of the underlying sky (and possibly galaxy) background. To achieve this, we constructed a custom Python-based GUI which allows the user to manually select spaxels containing the target SN ('object' spaxels) and spaxels used to determine the background ('sky' spaxels, which may contain some galaxy signal). The background spectrum is determined as the median spectrum across all 'sky' spaxels, and this median spectrum is subtracted from each 'object' spaxel. The final SN spectrum is then the sum of the sky-subtracted object spaxels, and the variance spectrum is the sum of the variance from all object spaxels (with no subtraction of sky variance).

This SN spectrum extraction technique produces excellent quality sky subtraction due to the robust spatial flat-fielding achieved with PyWiFeS. However, some obvious sky subtraction residual features are evident in the redder wavelengths of most R3000 spectra where the night sky exhibits sharp emission features from rotational transitions of atmospheric OH molecules. The intrinsic line width of these emission lines is below the resolution of the spectrograph, meaning the observed line width is that of the spectrograph—which in this case is only slightly larger than the detector pixel size. The natural wavelength solution of the spectrograph shifts spaxel-to-spaxel, so when all spaxels are resampled onto the same wavelength grid this means sky lines experience pixel-wise resampling that is not uniform across the full instrument field of view. Thus, when a median sky spectrum is subtracted from a specific spaxel, some residual features arise due to this resampling effect. A more robust technique for correcting this would be to model the intrinsic sky spectrum using the multiple samplings achieved across all spaxels and resample it to the wavelength solution of each spaxel before subtracting it (as was demonstrated for two-dimensional spectroscopic data by Kelson 2003). Such a technique is beyond the scope of the current data release, but is being prioritised for future AWSNAP releases.

2.2. Long-term behaviour of the WiFeS instrument

One key advantage of having a long-running observing programme is the ability to characterise the long-term behaviour of the WiFeS instrument. Below we analyse the stability of the wavelength solution and instrument throughput on multi-year timescales. WiFeS did undergo a major change in early 2013 when the detectors for both arms of the spectrograph were replaced with higher throughput E2V CCDs. Thus, we restrict our analysis to dates from late 2013 May until the end of the current data release in 2015 August.

We collected the wavelength solution fits for the B3000 (R3000) grating from 48 (45) distinct epochs following the WiFeS detector upgrade. In Figure 1, we plot the difference between the wavelength solution for each individual epoch and the mean wavelength solution across all epochs. Epochs are colour-coded from earliest (red) to latest (purple) to illustrate potential coherent long-term shifts in the wavelength solution. The top panels present the B3000 grating, whilst the bottom panels present the R3000 gratings. The left and middle columns represent the WiFeS slitlets at the top and middle of the detectors, respectively. In the right hand panels of this Figure, we show the average deviation of the wavelength solution for a given epoch from the global mean wavelength solution, as a function of epoch. This allows us to track any coherent evolution of the detector wavelength solution with time.

From these plots, we see clear demonstration of the remarkable stability of the WiFeS instrument. The RMS

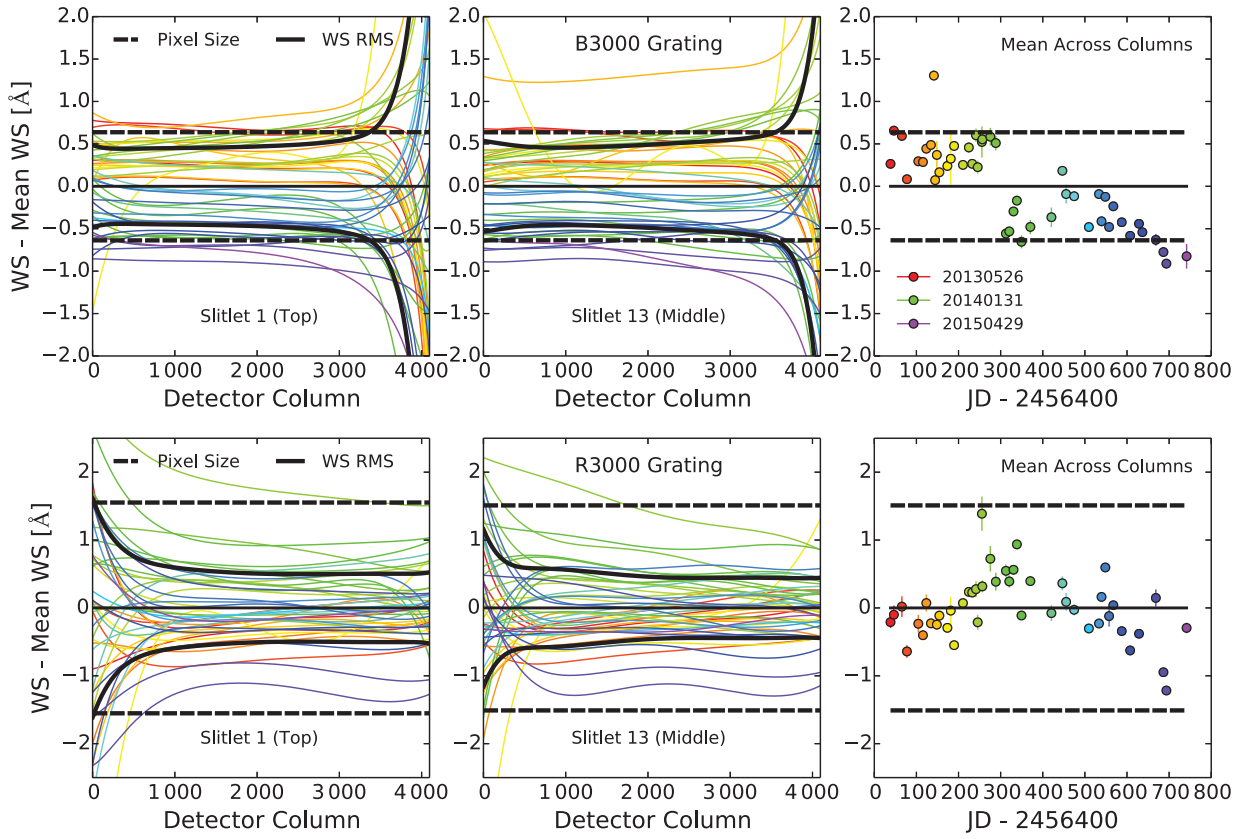

Figure 1. Evolution of the WiFeS wavelength solution over a 2-yr period spanning 2013 May to 2015 April. In the left two panels of each row, we plot the deviation of individual wavelength solutions from the mean solution (averaged over the full 2-yr period) for the top and middle slitlets of the instrument (left and middle columns, respectively) for the B3000 (top row) and R3000 (bottom row) gratings. Wavelength solution residuals are colour-coded by date from earliest (red) to latest (purple), with the pixel size (dashed black lines) and wavelength solution residual RMS (solid black lines) displayed for comparison. In the right panels of each row, we show the average deviation (across all wavelengths) from the mean wavelength solution as a function of epoch, to trace the temporal evolution of the instrument solution (points for individual epochs obey the same colour scheme as the left panels).

variation of wavelength solution is smaller than a single pixel for both gratings (i.e. both detectors) for nearly all wavelengths, with the exception of the lower throughput regions near the dichroic boundary. There is some evidence of a coherent shift of the blue detector wavelength solution over the 2-yr time period probed here, but this is still less than two pixels shift. For the red detector, we can say confidently that *the wavelength solution has shifted by less than a pixel over a timescale of 2 yrs*. This remarkable stability achieved (by design) by WiFeS means the use of the wavelength solution from an adjacent night yields negligible changes in wavelength, and thus small instrumental velocity shifts—highly suitable for supernova analyses.

We then collected illumination corrections (derived from twilight flat observations) from 46 (45) distinct epochs for the B3000 (R3000) grating. In Figure 2, we show the mean illumination correction (left panels) and RMS of the illumination correction (right panels—presented in fractional form, i.e. the RMS divided by the mean) for both the B3000 (top) and R3000 (bottom) gratings. We find the mean variation of the illumination correction to be 1.4 and 1.2% for the B3000 and R3000 gratings, respectively, for the full WiFeS field of view. The nature of the instrument optics are such that the outer regions of instrument field of view have slightly lower throughput, and thus a higher fractional RMS than the inner most region. For the innermost 8 arcsec × 8 arcsec region typically used for SN observation in AWSNAP, the RMS of the illumination correction is 0.8 and 0.3% for the blue and red detectors (i.e. B3000 and R3000 gratings). Thus, the throughput of the WiFeS instrument has remarkable spatial uniformity on long (multi-year) timescales.

2.3. Observing conditions at siding spring observatory

In addition to the long-term behaviour of the WiFeS instrument, our observing programme allows us to monitor the observing conditions at Siding Spring Observatory. Below we briefly discuss the atmospheric throughput and seeing conditions experienced during AWSNAP observing.

We collected the flux calibration solutions from 59(54) epochs for the B3000 (R3000) grating from 2013 May to

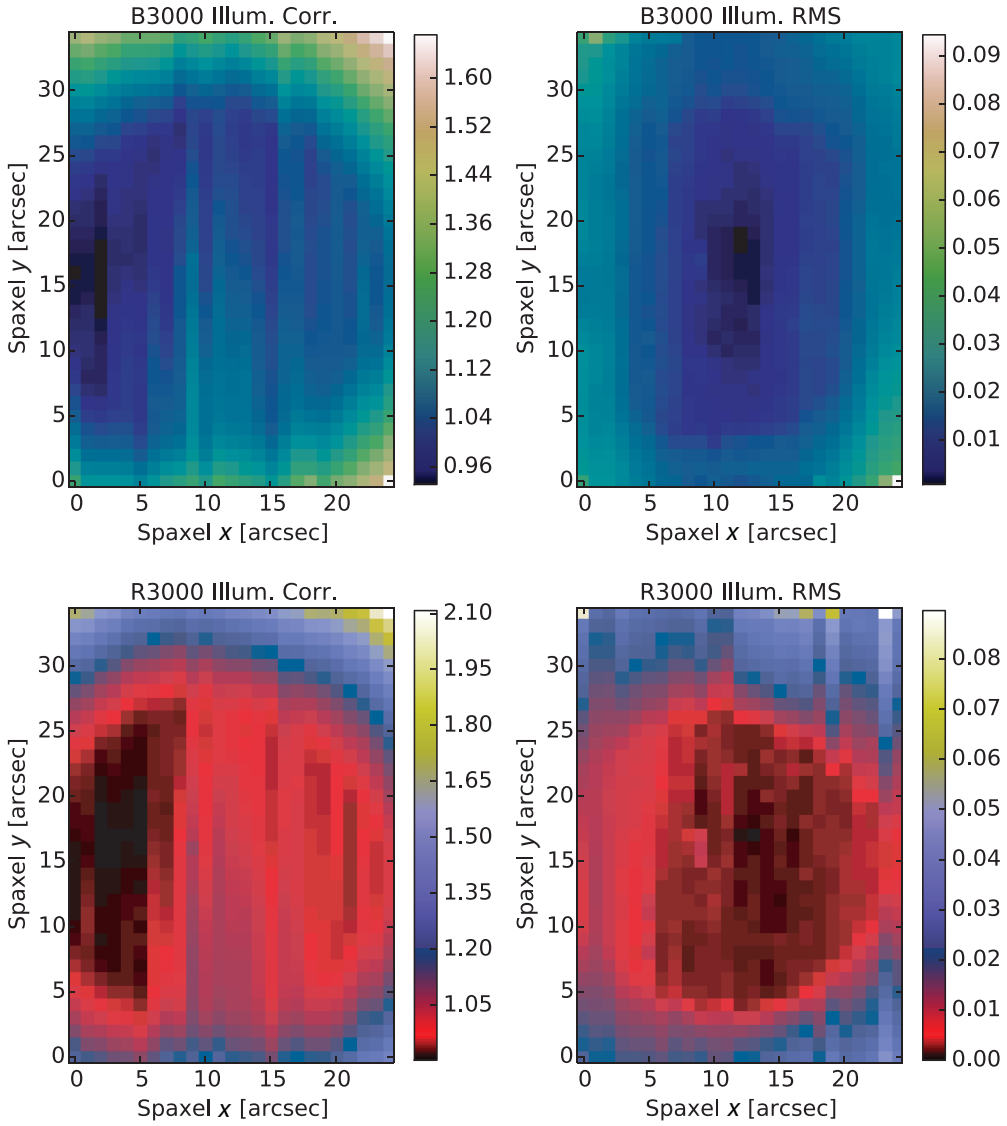

Figure 2. The normalised mean (left column) and RMS (right column) of the illumination corrections for the B3000 (top row) and R3000 (bottom row) gratings. The RMS images are shown as fractional values of the mean illumination correction.

2015 August, and these are plotted in Figure 3 after being normalised in the wavelength range with highest throughput (45 00–5 400 Å and 6 500–8 000 Å for B3000 and R3000, respectively). These curves represent the normalised throughput (in magnitudes) of the instrument and atmosphere as measured with spectrophotometric standard stars (typically from Oke 1990; Bessell 1999; Stritzinger et al. 2005) whose flux has already been corrected using the nominal Siding Spring extinction curve from Bessell (1999). The effects of the instrument throughput and atmospheric transmission are degenerate here, as WiFeS instrument throughput cannot be independently measured using local (i.e. terrestrial) calibration sources.

From the curves in Figure 3, we see that the total combined throughput of the instrument plus atmosphere is relatively stable. We calculated the RMS colour variation in the throughput curves and find variations of $\sigma(U-B) = 0.09$ mag for B3000 (note the V band runs into the wavelength range where the dichroic splits light between the blue and red channels) and $\sigma(r-i) = 0.04$ mag for R3000. We note these are calculated from the mean flux calibration solution for each night, where no attempt has been made to derive a unique extinction curve for a given night. These colour variations are relatively small, and comparable in size to the colour dispersion found when comparing spectrophotometry to imaging photometry for other SN spectroscopy samples (e.g. Silverman et al. 2012c; Blondin et al. 2012; Modjaz et al. 2014).

We also measured the atmospheric seeing during our observing programme, using both guide star FWHM measurements recorded from the WiFeS guider camera and low airmass ($secz \leq 1.5$) WiFeS data cubes convolved with the B- and R-band filter curves (for the blue and red cameras,

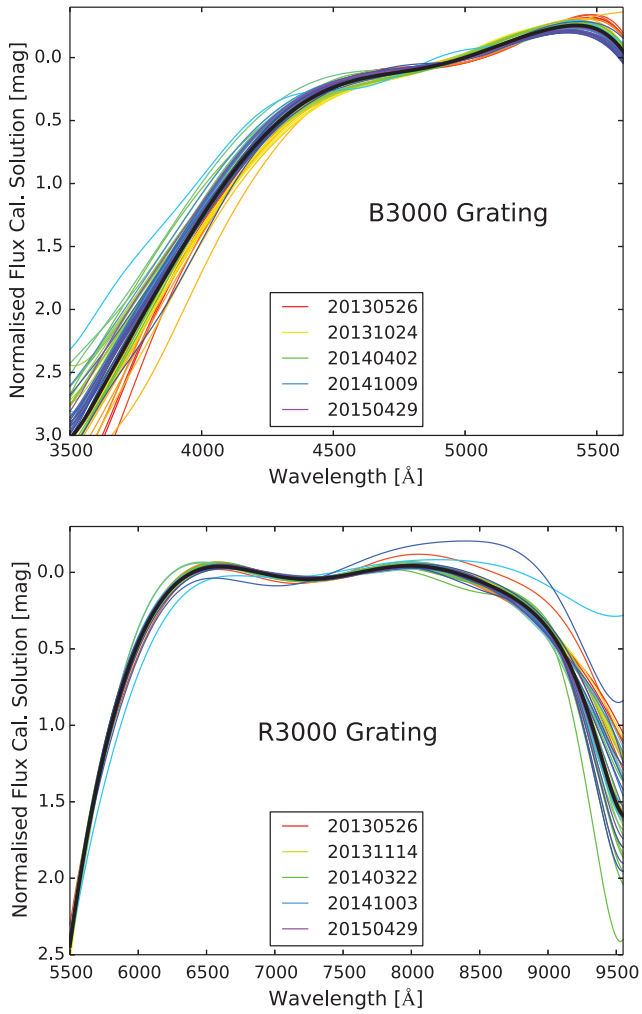

Figure 3. Flux calibration solutions for the B3000 (top) and R3000 (bottom) gratings. As in Figure 1, these are colour-coded by date from earliest (red) to latest (purple), with the mean flux calibration solution shown as the solid black line.

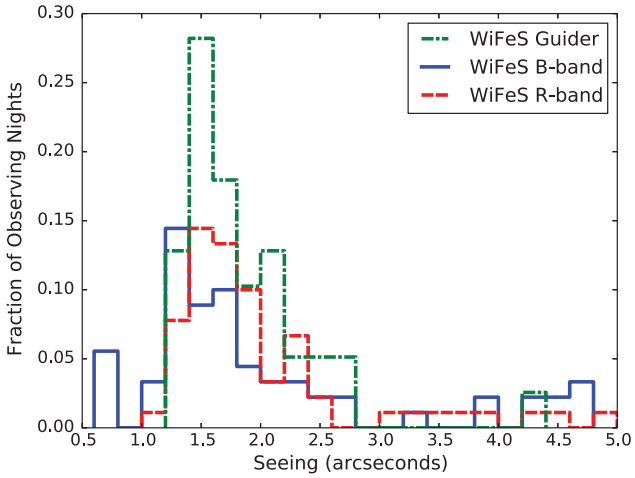

Figure 4. Seeing measurements at Siding Spring Observatory as measured during AWSNAP observations. These include measurements from the WiFeS guider camera (green dash-dot histogram), and measurements of low airmass standard star WiFeS datacubes convolved with *B*-band (blue solid histogram—from the blue detector) and *R*-band (red dashed histogram—from the red detector) filter curves.

respectively). We plot the observed distribution of seeing values in Figure 4. The seeing distribution peaks slightly above 1.5 arcsec (for all measurements) with a tail predominantly filled to 2.5 arcsec, with little or no sub-arcsecond observations and a small number of observations with incredibly poor seeing (3.0 arcsec or greater).

3 THE AWSNAP SUPERNOVA SAMPLE AND SPECTROSCOPIC DATA RELEASE

In this Section, we briefly describe the global characteristics of the sample of SNe comprising the first data release (DR1) for AWSNAP. This consists of observations made between 2012 July18 and 2015 August17, a total of 357 epochs of 175 total SNe. These spectra have all been uploaded to WISeREP (Yaron & Gal-Yam 2012), with most made publicly available and the small remainder set to be made public with the associated PESSTO publication within the next year. Some additional spectra taken after 2015 August 17 have been processed and released via WISeREP, and we expect the future release of AWSNAP spectra to proceed in a continuous fashion via the same procedures outlined in this work.

AWSNAP originated as the spectroscopic observation programme for the supernova group at the ANU. The programme was intended to cover a broad range of science topics driven by transient discoveries from contemporaneous photometric surveys, with a large emphasis on timely classification of newly discovered transients. The observing and target selection strategy for AWSNAP was heavily influenced by the scheduling of our observing time, which typically consisted of one single classically scheduled full night of observing every 8–15 d throughout the entirety of the calendar year. The most significant implication of this scheduling was that dense spectroscopic sampling (i.e. 2–3 d cadence) was generally not viable for our preferred targets (though on rare occasions we requested time exchange with other observers for targets of particular importance). Furthermore, additional targets were always needed to fill an entire night of observing. Thus, we frequently chose to make complementary observations of targets being observed through the PESSTO programme (Smartt et al. 2015), or chose targets whose spectroscopic data would have legacy value for future analyses. As a result, we observed a diverse range of targets that covered the entire Southern sky. The full list of targets and their classification information in presented in Table A1 in Appendix A, and their distribution on the sky is shown in Figure 5.

The AWSNAP spectra have relatively high signal-to-noise (S/N) by design so that they might be useful for precision spectral feature measurement. Our sample's median S/N is 16 per Å, with 1σ high and low S/N values of 40 and 6 per Å, respectively. We show some example AWSNAP spectra in

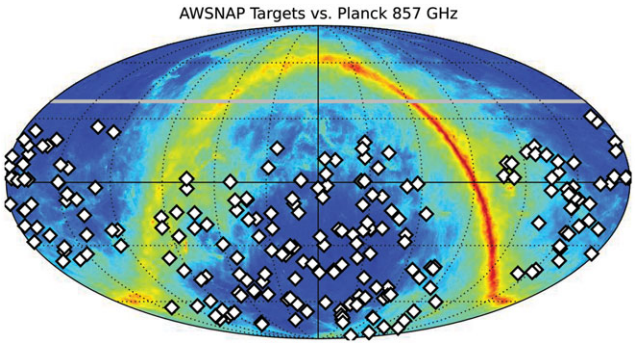

Figure 5. On-sky distribution (in equatorial coordinates) of all extragalactic targets in AWSNAP DR1 (white diamonds) plotted over the 857 GHz all-sky map from the *Planck* satellite (Planck Collaboration et al. 2011) which reveals emission by Milky Way dust. The physical pointing limit of the ANU 2.3-m telescope ($\sim +40^\circ$ declination) is shown as the solid gray bar.

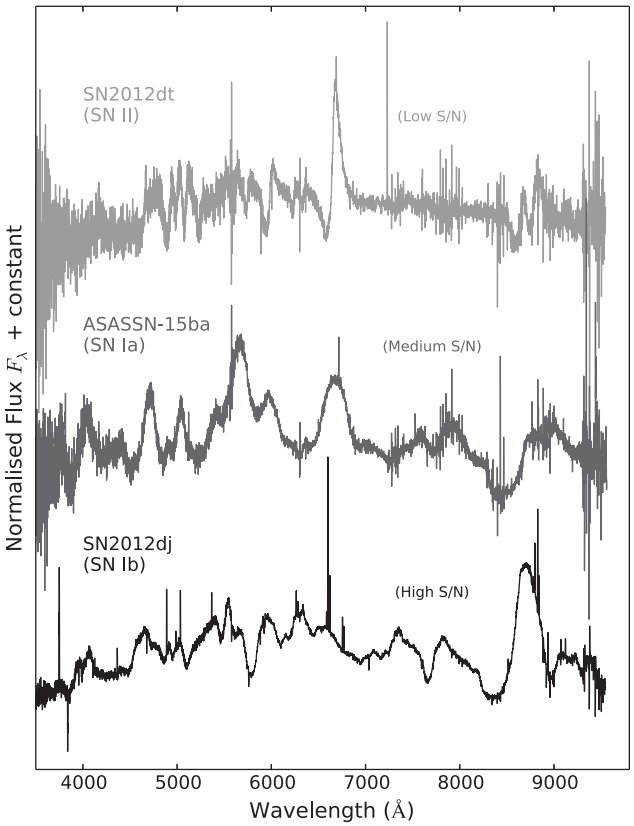

Figure 6. Example spectra spanning the typical range of signal-to-noise (S/N) in the AWSNAP sample. Shown here are spectra of SN 2012dt (a SN II, with a 'low' S/N of 5 per Å), ASASSN-15ba (a SN Ia, with a 'medium' S/N of 13 per Å), and SN 2012dj (a SN Ib, with a 'high' S/N of 33 per Å).

Figure 6 exhibiting low (-1σ), medium (median), and high ($+1\sigma$) S/N.

In Figure 7, we present a histogram of the number of spectroscopic observations per target for the AWSNAP sample compared to three major SN Ia spectroscopic data releases: the Berkeley SN Ia Programme (BSNIP; Silverman et al. 2012c), the Harvard Center for Astrophysics (CfA) Supernova Programme (Matheson et al. 2008; Blondin et al. 2012), and the Carnegie Supernova Project (CSP; Folatelli et al. 2013). Our sample has a high fraction of singly observed targets compared to the other programmes. This is in part due to the fact that our data release includes all our SN classification spectra, as well as the persistent need for us to fill our classically scheduled observing queue. We thus also show in the inset of Figure 7 the normalised histogram of spectroscopic epochs for multiply observed SNe (i.e. targets with $N_{\rm obs} > 2$), which shows a much more similar distribution to the other programmes.

Table 2. AWSNAP objects and spectra by SN type.

SN type	# Objects	# Spectra
SN Ia	101	180
SN II	53	117
SN Ibc	15	43
SLSN	6	17
Total	175	357

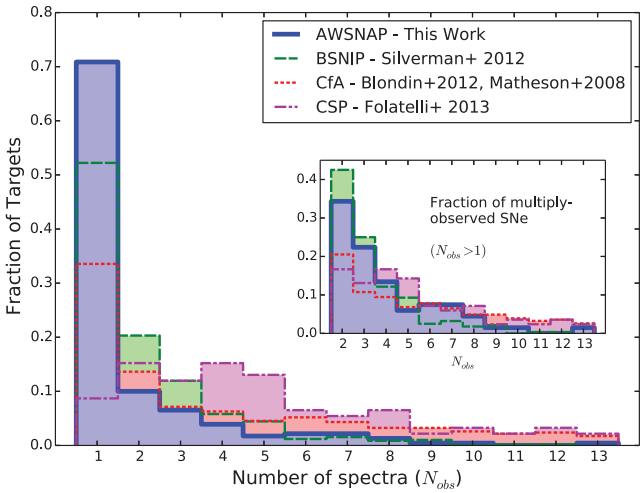

Figure 7. Normalised histogram of the number of spectroscopic epochs per target for the full sample of AWSNAP DR1 targets. For comparison, we also show the same histogram for previous SN spectroscopy surveys: BSNIP (Silverman et al. 2012c), CfA (Matheson et al. 2008; Blondin et al. 2012), and CSP (Folatelli et al. 2013). The inset shows the (re-)normalised histograms of the number of spectroscopic epochs for multiply observed targets (i.e. those with $N_{\rm obs} > 1$) in the same surveys.

The types of SNe observed in AWSNAP DR1 is summarised in Table 2 and presented graphically in Figure 8. We show both the number of targets and number of spectra for AWSNAP, and for reference we compare this to the magnitude-limited rates for SNe in the local universe calculated by Li et al. (2011a). For this figure, we have grouped the SNe by type into four main categories:

- SNe Ia: includes the standard (Branch-normal) SNe Ia, sub-luminous (SN 1991bg-like Filippenko et al. 1992a), over-luminous (SN 1991T- and SN 1999aa-like

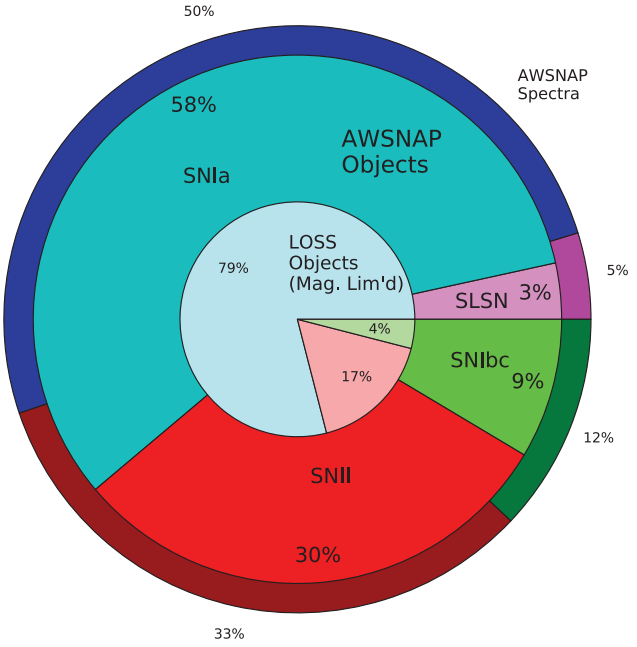

Figure 8. Total number of spectra (outer ring) and SN targets (middle annulus) for AWSNAP broken down by SN type, compared to the volume-limited SN rates (inner circle) for the LOSS survey (Li et al. 2011a, —note this galaxy-targeted survey did not find any SLSNe). In each ring, the regions are colour-coded by (broad) SN type (see text for discussion): SNe Ia (blue), SNe II(red), SNe Ib/Ic (green), and SLSNe (purple).

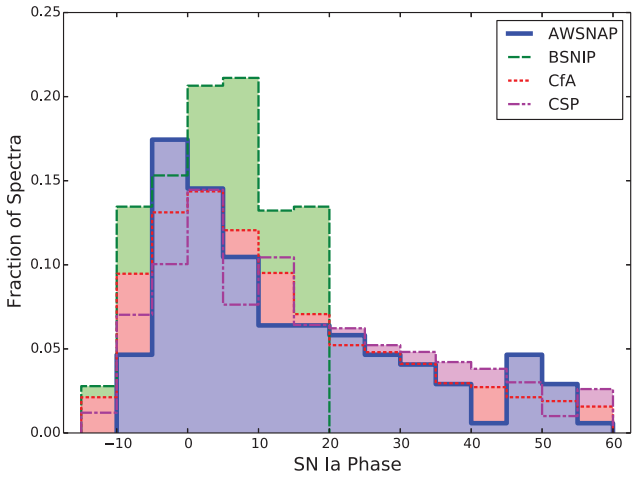

Figure 9. Histograms of spectroscopic phases (with respect to *B*-band maximum light) for SN Ia spectra in AWSNAP and other SN Ia spectroscopy samples (the same as in Figure 7). Note the AWSNAP phases are based on the spectroscopic-based phase reported with the SN classification, which may have an associated uncertainty of 3–5 d.

Filippenko et al. 1992b), candidate 'super-Chandrasekhar' SNe Ia (Scalzo et al. 2010, 2012), and SNe Iax (Foley et al. 2013).

- SNe Ibc: SNe Ic, SNe Ib, and SNe IIb—the standard classes of 'stripped-envelope' SNe (e.g. Bianco et al. 2014; Modjaz et al. 2014; Graur et al. 2015; Liu et al. 2016).
- SNe II: SNe IIP and SNe IIL—which we note cannot be distinguished spectroscopically—and SNe IIn.
- SLSNe: 'superluminous' SNe—for our sample, this consists entirely of the 'SLSN-Ic' type (see, e.g. Inserra et al. 2013) which show blue continua with weak absorption features and no hydrogen signatures.

We note these groupings are made strictly to provide broad perspective on the sample statistics, but we reiterate that the SN sub-types within each group have their own unique physical mechanisms.

From Figure 8, we clearly see that, as expected, SNe Ia comprise the majority of objects and spectra in the AWSNAP sample, but comprise a smaller fraction than might be expected from a pure magnitude limited sample of SNe such as that of the Lick Observatory Supernova Search (LOSS, whose relative SN rates are presented in Li et al. 2011a). This may be due in part to the fact that many of the SNe in AWSNAP were discovered by untargeted supernova searches such as the ASAS-SN (Shappee et al. 2014). These surveys find SNe in low-mass galaxies that are missed by targeted surveys such as LOSS. Due to the increased star-formation intensity in low-mass galaxies (e.g. Salim et al. 2007), this means the relative rate of core-collapse SNe will be higher and thus CCSNe will comprise a higher fraction of the sample. Additionally, we explicitly targeted a higher fraction of CCSN discoveries owing to the comparative paucity of CCSN spectroscopic samples compared to SNe Ia (again arising from the magnitude-limited rates). Thus, our higher representation of CCSNe than the expectation from the magnitude-limited rates of Li et al. (2011a) is likely a combination of the higher CCSN fraction for our untargeted feeder surveys and our explicit emphasis on preferential targeting of CCSNe.

4 TYPE IA SUPERNOVA SPECTRA FROM AWSNAP

As a first demonstration of the usefulness of the AWSNAP dataset, we analyse basic spectroscopic features of the SNe Ia in our sample—this comprises 180 total spectra of 101 objects. In Figure 9, we plot a histogram of the phases[2] of our SN Ia spectra, again compared to previous large SN Ia spectroscopy surveys (CfA, BSNIP, CSP). Our sample shows a similar phase coverage as previous surveys, with perhaps a slight increase in earlier phases due to improved SN discovery efficiency from nearby SN searches. In the sections that follow, we further analyse features of interest from the AWSNAP SN Ia spectroscopy sample.

4.1. Spectral features in SNe Ia at maximum light

We begin by inspecting the spectra of SNe Ia close to the epoch of peak brightness. These maximum light spectra have

[2] Based on the spectroscopically estimated phase reported at the time of classification.

a long history of providing key insights into the diversity of SN Ia explosions through the study of 'spectral indicators' (Nugent et al. 1995; Hatano et al. 2000; Benetti et al. 2005; Bongard et al. 2006, 2008; Hachinger, Mazzali, & Benetti 2006; Hachinger et al. 2008; Branch et al. 2006; Branch, Dang, & Baron 2009; Bronder et al. 2008; Silverman, Kong, & Filippenko 2012b), as well as potential avenues for improving the cosmological standardisation of SNe Ia (Wang et al. 2009; Bailey et al. 2009; Blondin, Mandel, & Kirshner 2011; Silverman et al. 2012a). Thus, we actively targeted many SNe Ia (which had already been classified) on an epoch close to maximum light to obtain high-quality spectra facilitating such studies.

We isolated the sample SNe Ia with a spectrum within 5 d of estimated peak brightness. It is important to reiterate here that the phases for our SN Ia sample are extrapolated from the reported spectroscopic classification phase and date. It has been demonstrated previously (e.g. Blondin et al. 2012) that the phase determined for SNe Ia via spectroscopic matching codes such as SNID (Blondin & Tonry 2007) typically has an uncertainty of at least 3–5 d. Thus, we may have included SN Ia spectra as much as 10 d removed from maximum light. Our analysis here is intended to be illustrative of the utility of our published spectra, and more detailed quantitative spectroscopic analyses should always be coupled to a robust photometric data set.

For the analysis that follows, we measure two key quantities of interest: the silicon absorption ratio $R_{\rm Si}$, and the strength of high-velocity features (HVFs) $R_{\rm HVF}$. For this work, we define $R_{\rm Si}$ as the ratio of the pseudo equivalent width (pEW) of the 5962 Å feature to the pEW of the 6355 Å feature. The pEW for each feature is measured by fitting a linear pseudo-continuum across narrow regions redward and blueward of the given feature (similar to methods employed in Silverman et al. 2012b), then integrating the flux in the normalised absorption feature.

$R_{\rm Si}$ is known to correlate strongly with the SN Ia light curve decline rate (Nugent et al. 1995). We quantified the relationship between our definition of $R_{\rm Si}$ (the pEW ratio) and light curve decline rate Δm_{15} by fitting a linear relationship between these quantities for a sample of 342 SNe Ia collated from the CfA, BSNIP, and CSP samples. The fit to these data is presented in Appendix A2, shown graphically in Figure A1 with a best fit trend given by Equation (A1). Below we will use this relation to display the corresponding range of Δm_{15} spanned by our observed values of $R_{\rm Si}$.

We measure the HVF strength for our SN Ia sample using the same techniques employed in Childress et al. (2014b), and similarly define $R_{\rm HVF}$ as the ratio of the pEW of the HVF to the pEW of the photospheric velocity feature (PVF). Briefly, we first normalise the Ca NIR feature using a linear pseudo-continuum fit. We then fit the Ca NIR feature with two Gaussians in *velocity space* with velocity centres, widths, and absorption depths fitted with a Python `mpfit` routine. Each component in velocity space corresponds to a triplet in wavelength space, and we set the absorption depth of each component equal to each other (i.e. the optically thick limit). As in Childress et al. (2014b), we require the photospheric velocity component to have a velocity centre within 20% of the value derived for the Si 6355 Å feature, though in most cases the results are the same if this requirement is removed.

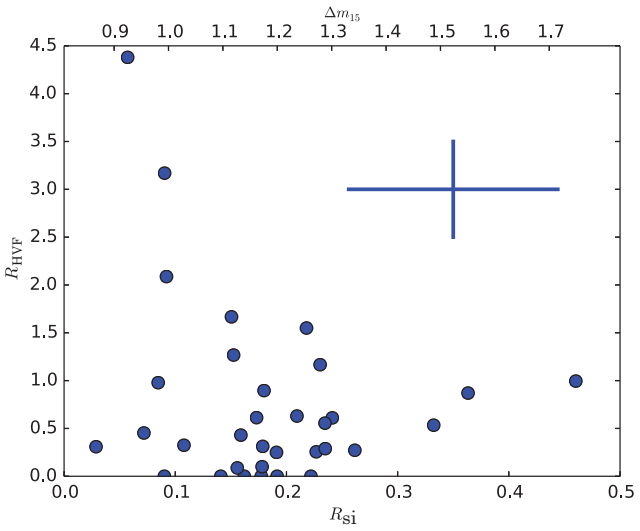

Figure 10. Strength of the high-velocity features (HVFs) in the Ca II NIR triplet—using the quantity $R_{\rm HVF}$ as defined by Childress et al. (2014b)—plotted against the Si II absorption strength ratio $R_{\rm Si}$ defined by Nugent et al. (1995). On the top axis, we show the rough equivalent light curve decline rate Δm_{15} values corresponding to the range of $R_{\rm Si}$ values. The crosshair in the upper right represents the characteristic errors in measurement of $R_{\rm HVF}$ (typically 20%, plotted here for the larger values of $R_{\rm HVF}$) and the error in Δm_{15} when converted from $R_{\rm Si}$.

In Figure 10, we plot the measured HVF strength ($R_{\rm HVF}$) versus the silicon absorption strength ratio $R_{\rm Si}$. For illustrative purposes, we also show the scale of light curve decline rate Δm_{15} corresponding to the plotted range of $R_{\rm Si}$ using the above relation. A representative error bar for Δm_{15} from the above relation and a typical $R_{\rm HVF}$ error-bar are shown in the figure.

Figure 10 demonstrates a tendency for SNe Ia with strong HVFs to also have low values of $R_{\rm Si}$ and thus broad light curves (low Δm_{15}). This correlation of HVFs with SN Ia light curve width was first observed by Maguire et al. (2012) in composite high-redshift SN Ia spectra, and subsequently confirmed by numerous studies of low-redshift SNe Ia (Childress et al. 2014b; Maguire et al. 2014; Pan et al. 2015; Silverman et al. 2015; Zhao et al. 2015). Our results support these studies with spectra alone.

4.2. Narrow sodium absorption features in SN Ia spectra

A great advantage of the higher resolution of WiFeS (compared to many spectrographs deployed for other SN spectroscopy surveys) is the ability to detect narrow absorption features, particularly the Na I doublet at λλ5890/5896 Å. This feature has a long history of being used to infer the

presence of foreground dust in SNe Ia (Barbon et al. 1990; Turatto, Benetti, & Cappellaro 2003; Poznanski et al. 2011; Poznanski, Prochaska, & Bloom 2012; Phillips et al. 2013). Earlier works attempted to derive correlations between SN Ia colours and sodium absorption strength (i.e. the absorption equivalent width), but Poznanski et al. (2011) showed sodium to be a poor indicator of SN Ia reddening. Phillips et al. (2013) refined this result by showing that SN Ia reddening exhibits a strong correlation with absorption strength of the diffuse interstellar bands (found exclusively in the interstellar medium) but some SNe Ia have an excess of sodium absorption that does *not* coincide with associated reddening of the SN. Thus, sodium features in SNe Ia remain instructive but should be considered with a measure of caution.

Recently, velocities of sodium absorption features in SN Ia spectra have been used as a diagnostic of CSM, including cases of some SNe Ia (Patat et al. 2007; Simon et al. 2009) where the sodium absorption features exhibit variability (though most do not—see Sternberg et al. 2014), indicating SN-CSM interaction. More recently, a statistical analysis of the velocity distribution of sodium features in SNe Ia by Sternberg et al. (2011) found an excess of SNe Ia with blueshifted sodium features, indicating that a fraction of SNe Ia explode inside an expanding shell of material that was presumably shed by the SN Ia progenitor system prior to explosion. Maguire et al. (2013) extended this work to show that the excess of SNe Ia with blueshifted sodium absorption was populated predominantly by the more luminous SNe Ia with slow declining light curves (i.e. high 'stretch').

We thus searched for the presence of sodium absorption features in our sample of SN Ia spectra. For most SNe Ia (13), this was done with the lower resolution (R3000) observations of the SN at maximum light. For six SNe Ia, we also had a higher resolution (R7000) observation of the SN at maximum light. In a few instances, this observation was triggered by the presence of strong reddening being reported in the SN classification announcement. For the other instances, we obtained both a low-resolution (R3000) and high-resolution (R7000) spectrum in the red whilst obtaining a longer exposure blue (B3000) spectrum during nights near full moon when the blue sky background was exceptionally high.

We fitted the sodium doublet absorption profile as follows. First, the spectrum was normalised to the local continuum by fitting a quadratic to the SN flux between 10–25 Å redward or blueward of the doublet centre (5893 Å). The absorption profile was fitted as two Gaussians with rest wavelengths set by the doublet wavelengths but with unknown (common) velocity shift and velocity width and (independent) absorption depths. This was done with an `mpfit` routine in Python, which accounts for variable covariances and returns the appropriate fit values and uncertainties. We show representative examples for fits to data from both gratings in Figure 11. The outcomes for our sodium profile fits are presented in Table A4 in Appendix A, and comprise six successful fits for targets with R7000 spectra, and 13 for R3000 spectra.

The primary quantity we wanted to measure from the sodium absorption feature was its velocity with respect to the local standard of rest at the SN site. The default local rest velocity was initially set to be the systemic velocity of the SN host galaxy. In some cases, we detected clear nebular emission lines at the SN site present in the SN spectrum—for these cases, the local rest velocity (i.e. the rotational velocity of the host galaxy at the site of the SN) was measured from the Hα emission line.

In two cases (SN 2014ao and ASASSN-14jg), no local Hα emission was present in the SN spectrum, and the SN sodium velocity differed from the host systemic velocity by more than 100 km s^{-1}. To obtain the true local rest velocities for these two SNe Ia, we took advantage of the integral-field data provided by WiFeS, which allows us to measure host galaxy properties (such as velocity) over a broad field of view.

We illustrate this for SN 2014ao in Figure 12: The WiFeS field of view extends from the host galaxy core to the outer edge of its spiral arms in the direction of the SN. We were able to extract the velocity of an H II region along the SN-host axis and found its velocity differed significantly from that of the host core ($\Delta v = 174 \pm 10$ km s^{-1}). As galaxy velocity curves tend to flatten at large radii, we use the H II region velocity as the local rest velocity of SN 2014ao—a value much closer to the measured sodium absorption velocity.

With the final sodium absorption velocities for our sample, we can inspect the relationship between sodium velocity and other spectroscopic properties of our SN Ia sample. In Figure 13, we plot the silicon absorption ratio ($R_{\rm Si}$), the HVF absorption strength ($R_{\rm HVF}$), and the absorption strength (i.e. equivalent width) of sodium itself against the velocity of the sodium absorption feature. Based on results of Maguire et al. (2013), we would expect SNe Ia with low $R_{\rm Si}$ and high $R_{\rm HVF}$ values (the high stretch, slow declining SNe Ia) to have a slight excess of blueshifted sodium absorption. Our sample size here is too small (and not well-selected) to make any robust statement about such preferences. However, we note that this analysis was not the explicit objective of our observations, but instead was a supplemental outcome facilitated by the nature of the WiFeS data.

Thus, WiFeS is an excellent instrument for measuring sodium absorption in SNe Ia, a key observable for investigating SN Ia progenitor systems. This is particularly true for observations taken with the R7000 grating, which provides sodium velocity uncertainties of order a few km s^{-1}, thus enabling a robust classification of the SN as being 'blueshifted' or 'redshifted'. More importantly, perhaps, is the capability of WiFeS to observe a wide field of view around the SN. This enables a measurement of the local systemic velocity at the SN location, even in cases where emission from the host galaxy is weak at the SN location itself.

4.3. Spectroscopic evolution of SN 2012dn

The SN with the greatest number of spectroscopic epochs in AWSNAP is SN 2012dn, and we show its AWSNAP

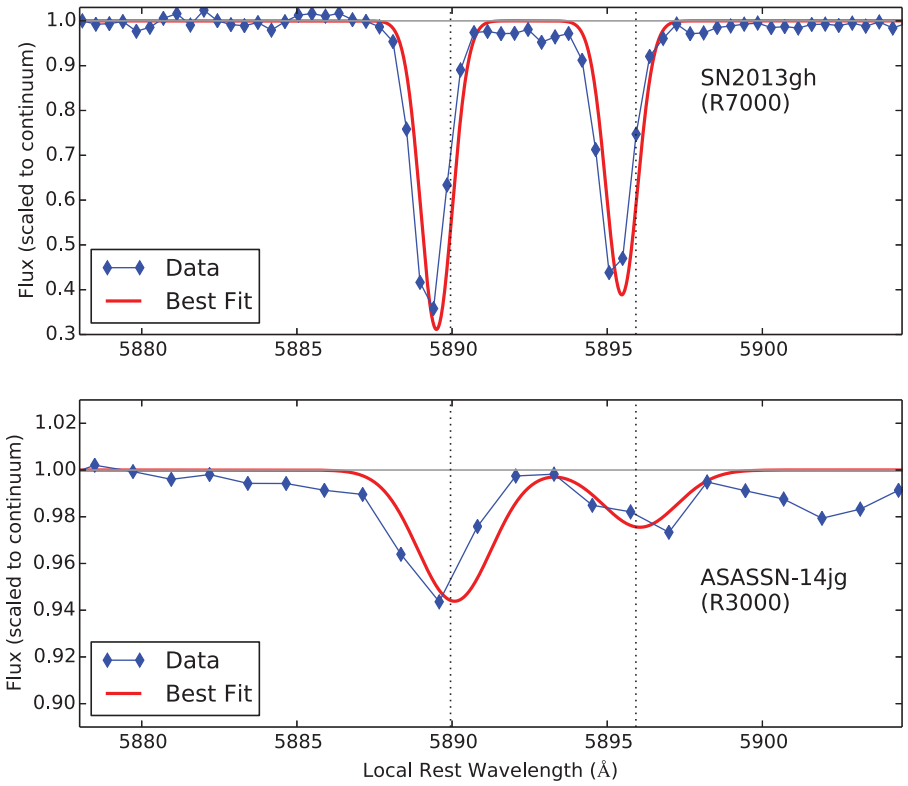

Figure 11. Sodium absorption fit examples for both the R7000 (top) and R3000 (bottom) gratings. Data (which have been normalised to the local continuum fit) are shown as blue diamonds whilst the best fit absorption profile is shown as the solid red curve. For reference, we also mark the continuum level (horizontal black line at value 1.00) and the rest wavelengths of the sodium doublet (vertical dotted gray lines).

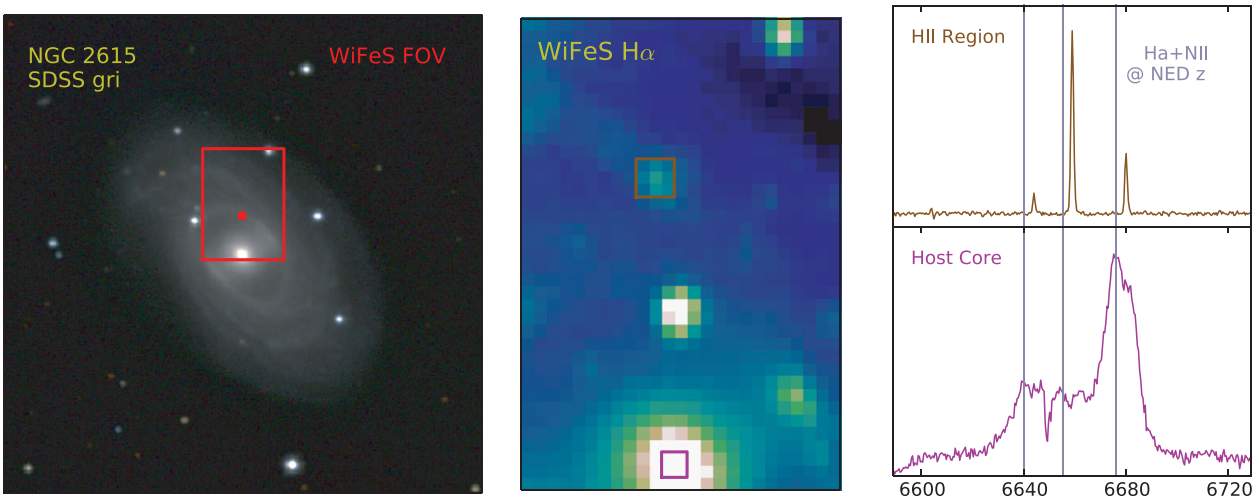

Figure 12. Determination of the local velocity for SN 2014ao in NGC 2615 with WiFeS. Left: SDSS (York et al. 2000) *gri* colour composite—created with SWARP (Bertin et al. 2002) and STIFF (Bertin 2012)—with the WiFeS field of view (red rectangle) and SN location (red dot) highlighted. Middle: Image of the SN 2014ao WiFeS data cube in the isolated wavelength range within ±6 Å (i.e. ±300 km s^{-1}) of the wavelength of Hα at the published redshift of NGC 2615, with host core (purple square) and nearby H II region (brown square) highlighted—the SN is the bright object near the centre. Right: Extracted WiFeS spectra of the nearby H II region (top) and host core (bottom) near the Hα+NII emission line group, with the expected location of those lines at the published redshift of NGC 2615 ($z = 0.014083$, Theureau et al. 1998a) shown as the vertical gray lines.

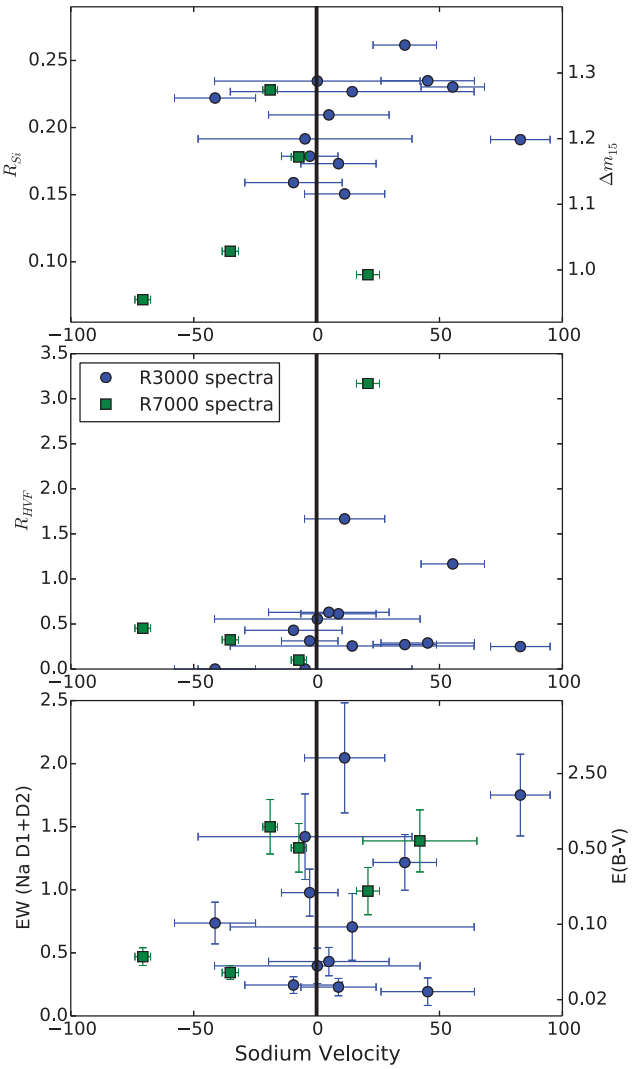

Figure 13. Top: Silicon absorption ratio $R_{\rm Si}$ plotted against velocity centre of the narrow sodium absorption feature (as in Figure 10 we show the corresponding values of Δm_{15}, though note the smaller range). Middle: HVF strength ($R_{\rm HVF}$) plotted against sodium absorption velocity. Bottom: Absorption equivalent width of the combined D1+D2 sodium lines plotted against sodium absorption velocity. On the right axis of this panel, we use the relation of Poznanski et al. (2012) to show the reddening values $E(B-V)$ corresponding to the measured sodium equivalent widths if the absorption arises solely from the ISM—though this is unlikely to be true for all SNe Ia (Poznanski et al. 2011; Phillips et al. 2013—see discussion in text). In all panels, higher resolution observations with the R7000 grating are displayed as green squares, whilst lower resolution R3000 observations are shown as blue circles.

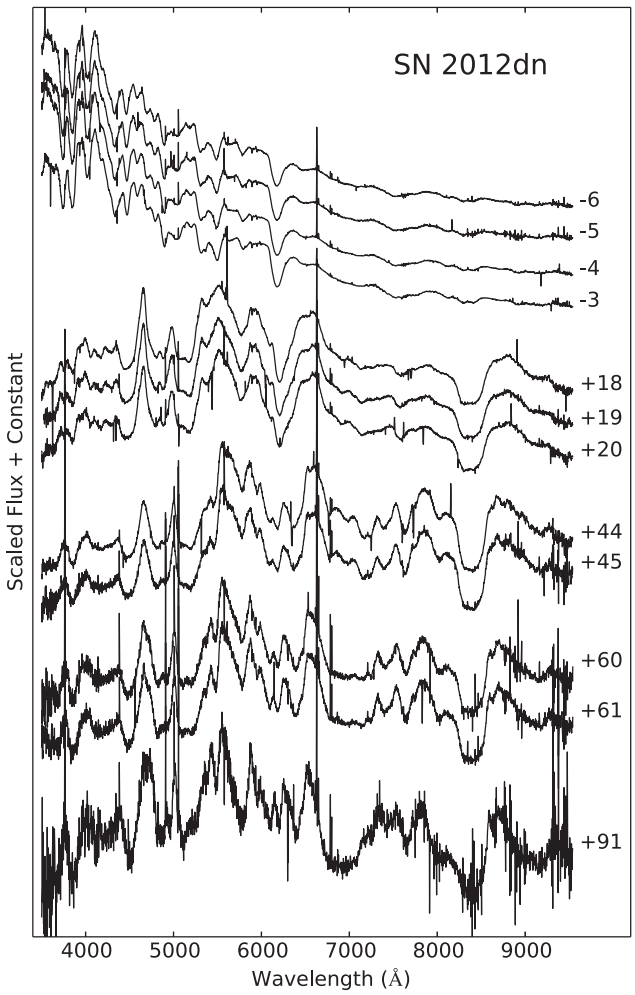

Figure 14. AWSNAP time series of SN 2012dn, labelled by phase with respect to the date of maximum light (2012 July 24, as determined by Chakradhari et al. 2014). Note these observations come from the first semester of AWSNAP when observing time was allocated in multi-night blocks separated sometimes by a month or more.

spectroscopic time series in Figure 14. SN 2012dn was a spectroscopically peculiar SN Ia whose photometric and spectroscopic evolution was studied extensively by Chakradhari et al. (2014)—they found it to be similar to the 'candidate super-Chandrasekhar' SN Ia SN 2006gz (Hicken et al. 2007). For brevity, we will refer to this class of objects as 'super-Chandra', though we caution the reader that the origin of the extreme luminosity of these objects is still under debate (see, e.g. Taubenberger et al. 2011; Hachinger et al. 2012). We comment on only a few additional outcomes for SN 2012dn from the AWSNAP data, but refer readers to Chakradhari et al. (2014) and Parrent et al. (2016) for a thorough discussion of this interesting object.

We obtained a very high signal-to-noise spectrum of SN 2012dn at phase +91 d (with respect to the date of maximum light 2012 July 24, as determined by Chakradhari et al. 2014). At this epoch, the SN is beginning to enter the nebular phase when the ejecta become optically thin, revealing emission from the iron group elements (IGEs) near the centre of the SN. Spectra at these epochs provide an excellent diagnostic of the nucleosynthetic products of the SN explosion. In Figure 15, we present our +91 d spectrum of SN 2012dn compared to very late spectra of other candidate super-Chandra SNe Ia SN 2007if (Scalzo et al. 2010; Yuan et al. 2010; Taubenberger et al. 2013) and SN 2009dc (Silverman et al. 2011; Taubenberger et al. 2011; Yamanaka et al. 2009; Tanaka et al. 2010; Hachinger et al. 2012; Kamiya et al.

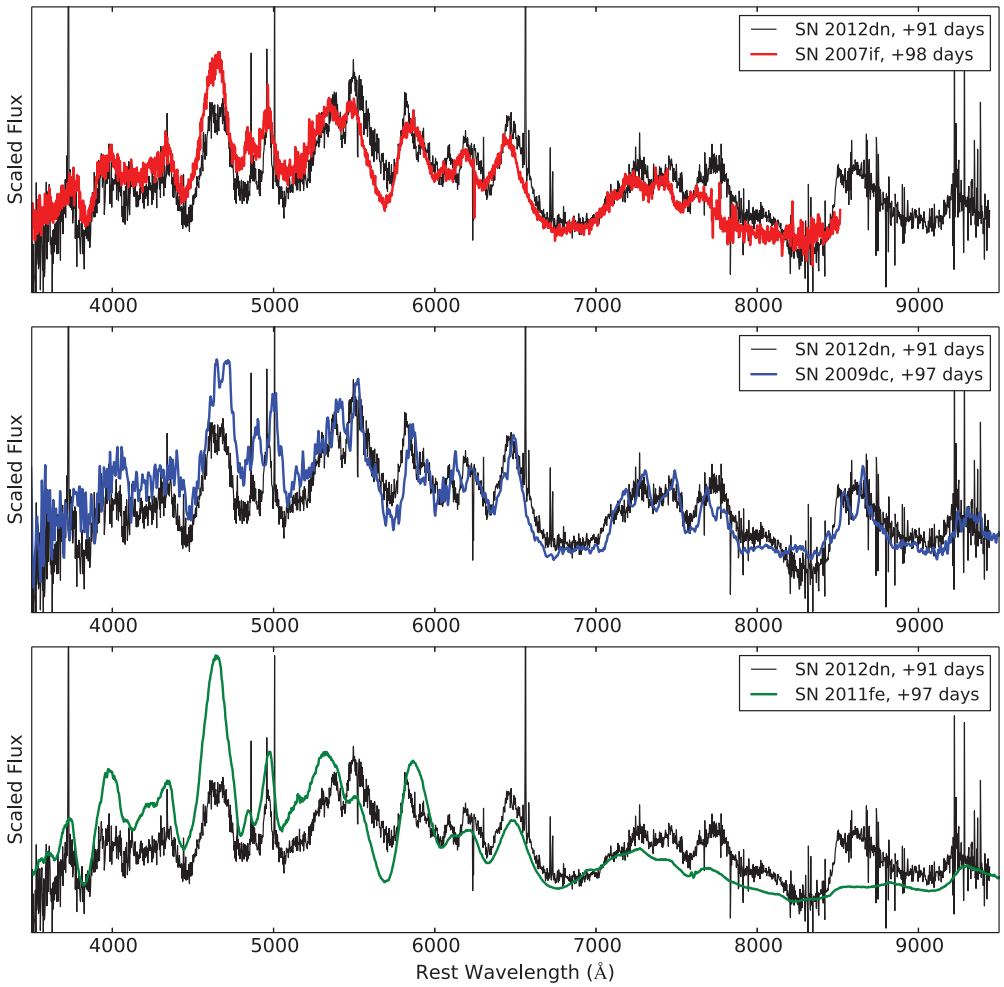

Figure 15. SN 2012dn at its latest AWSNAP epoch (+91 d on 2012 October 23) compared to other candidate super-Chandra SNe Ia SN 2007if at +98 d (top panel, from Silverman et al. 2011) and SN 2009dc at +97 d (middle panel, from Taubenberger et al. 2011), as well as the normal SN 2011fe (bottom panel, from Pereira et al. 2013).

2012; Taubenberger et al. 2013), as well as the gold standard normal SN Ia SN 2011fe (Nugent et al. 2011; Li et al. 2011b; Parrent et al. 2012; Pereira et al. 2013).

This comparison clearly reveals a strong spectroscopic similarity between SN 2012dn and the candidate super-Chandrasekhar SNe Ia, and a distinct dissimilarity with SN 2011fe. Perhaps, most prominent is the weaker Fe III line complex at ∼4 700 Å for the super-Chandra SNe Ia compared to SN 2011fe. This discrepancy is also evident in fully nebular spectra of super-Chandra SNe Ia at ∼1 yr past maximum light, as discussed by Taubenberger et al. (2013). This indicates that the ionisation state of the super-Chandra SNe Ia at these phases is different from normal SNe Ia—whether the diminished Fe III emission arises from a higher or lower average ionisation state remains uncertain.

Additionally, the velocity profile of the emission features in the super-Chandra SNe Ia exhibits a marked difference to that of SN 2011fe (and other normal SNe Ia). The normal SN Ia profile appears very Gaussian (and indeed is generally well fit by a Gaussian profile—Childress et al. 2015), whilst the super-Chandra velocity profile appears sharper at the centre. This is particularly evident for the line features at ∼5 900 and ∼6 300 Å, which at these epochs are dominated by Co III. Further spectral modelling of this and other late-phase super-Chandra spectra may reveal important insights into the structure and composition of the super-Chandra ejecta.

Finally, the high resolution of WiFeS reveals narrow emission lines from the host galaxy of SN 2012dn. We isolated the narrow host galaxy lines using the longest exposure of SN 2012dn, the late-phase observation of 2012 October 23 (+91 d). We fit a simple linear 'continuum' near each emission line by fitting a line to the SN spectrum between 5 and 15 Å away from the line centre on both the blue and red sides of the line. We illustrate this technique and present the SN-subtracted emission features in Figure 16.

In Table 3, we present the measured emission fluxes and errors for the major galaxy emission lines, all of which have been scaled by the observed flux in the Hβ line. By comparing the observed ratio of the Hα and Hβ lines to its expected value of 2.87 (the Balmer decrement Osterbrock & Ferland

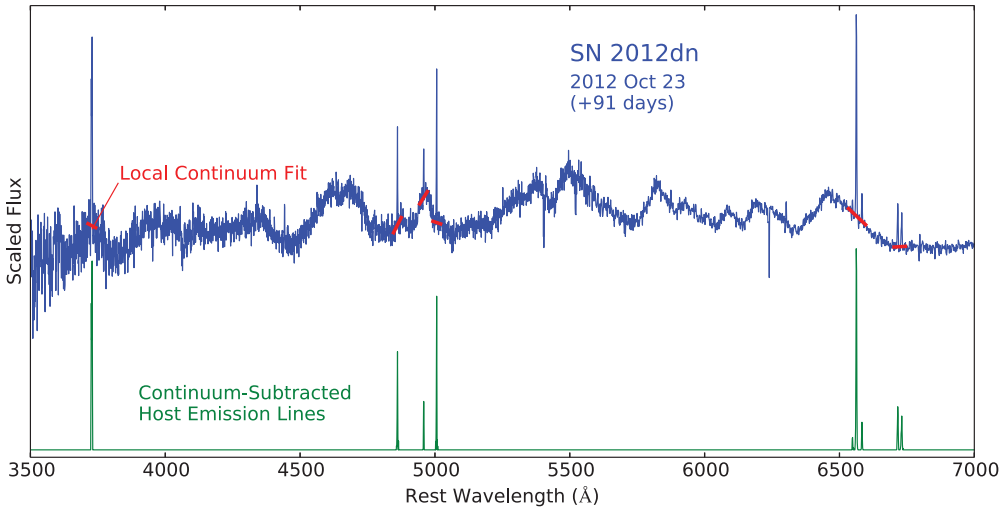

Figure 16. Extraction of host galaxy emission line flux (green) from late SN 2012dn spectrum (blue) using simple linear continuum fits (red).

Table 3. SN 2012dn local emission line fluxes.

Line	$F(\lambda)/F(H\beta)$ (raw)[a]	$F(\lambda)/F(H\beta)$ (de-reddened)[b]
[O II] λλ3727, 3730	3.61 ± 0.24	4.33 ± 0.29
Hβ	1.00 ± 0.10	1.00 ± 0.10
[O III] λ4959	0.45 ± 0.09	0.44 ± 0.09
[O III] λ5007	1.64 ± 0.10	1.60 ± 0.10
Hα	3.40 ± 0.07	2.87 ± 0.06
[N II] λ6548	0.06 ± 0.06	0.05 ± 0.05
[N II] λ6584	0.37 ± 0.06	0.31 ± 0.05
[S II] λ6717	0.71 ± 0.06	0.59 ± 0.05
[S II] λ6731	0.58 ± 0.06	0.48 ± 0.05

[a]Observer frame fluxes, scaled to Hβ.
[b]De-reddened using Balmer decrement reddening of $E(B-V) = 0.17$ so that $F(H\beta) = F(H\alpha)/2.87$ with a CCM reddening law, and scaled to the de-reddened flux of Hβ.

2006), we can determine the amount of reddening in the H II regions giving rise to the host emission lines. We use the Cardelli, Clayton, & Mathis (1989) to find a host reddening of $E(B-V) = 0.17 \pm 0.10$, a value remarkably similar to the SN reddening of $E(B-V) = 0.18$ (Milky Way plus host) determined by Chakradhari et al. (2014). We correct the host emission line fluxes for the value $E(B-V) = 0.17$ and report the corrected values (which we also re-scale to the de-reddened Hβ flux) in Table 3.

With the de-reddened host galaxy emission line fluxes, we calculate a gas-phase metallicity at the site of SN 2012dn. The N2 method of Pettini & Pagel (2004, hereafter PP04) yields $12 + \log(O/H) = 8.29 \pm 0.04$, whilst the O3N2 method of PP04 yields $12 + \log(O/H) = 8.35 \pm 0.03$. The former value is remarkably close to the estimated site metallicity for SN 2006gz of $12 + \log(O/H) = 8.26$ calculated by Khan et al. (2011) using the same metallicity method. If we convert the O3N2 value to the Tremonti et al. (2004) scale using the formulae of Kewley & Ellison (2008) as was done in Childress et al. (2011), we measure $12 + \log(O/H)_{T04} = 8.51 \pm 0.04$.

Comparing the above values to the solar oxygen abundance of $12 + \log(O/H)_{\odot} = 8.69$ (Asplund et al. 2009), we find the site metallicity for SN 2012dn is in the range 40–65% solar, depending on the chosen metallicity calibration. This sub-solar metallicity value is consistent with the previously reported trend for super-Chandra SNe Ia to prefer low metallicity environments (Taubenberger et al. 2011; Childress et al. 2011; Khan et al. 2011).

5 CONCLUSIONS

This work marks the primary data release for the AWSNAP, comprising 357 distinct spectra of 175 unique SNe. These data were collected using the WiFeS on the ANU 2.3-m telescope during 82 nights of observing over a 3-yr period from mid-2012 to mid-2015.

The AWSNAP spectroscopy sample is comparable in size to other SN spectra data releases, and its composition of SN types is roughly in line with expectations for a magnitude-limited SN search. The phase coverage of the AWSNAP SN Ia sample is comparable to other published SN Ia spectroscopy datasets (for SNe Ia with multiple epochs of observation), with the inclusion of more SNe Ia with a single observation (i.e. classification spectra only).

We presented some analyses of the AWSNAP SN Ia sample, including some results uniquely enabled by the fine wavelength resolution available with WiFeS. We measured broad absorption features in SN Ia spectra at maximum light, including the ratio of silicon absorption features $R_{\rm Si}$ and the strength of HVFs $R_{\rm HVF}$. Additionally, we measured the strength and velocity of narrow sodium absorption features, including some cases where the integral-field nature of the

instrument allowed us to measure the local systemic velocity within the SN host galaxy. Some expected feature trends, such as a correlation between R_{HVF} and R_{Si}, were recovered in our data set. The nature of sodium absorption in our sample was limited by small number statistics. Finally, we presented our observations of the candidate super-Chandrasekhar SN Ia SN 2012dn, and used narrow host galaxy emission features to show the SN site exhibits sub-solar metallicity.

The WiFeS instrument presents several unique advantages for the study of transients, particularly owing to its comparatively narrow velocity resolution ($\sigma_v \sim 45\,km\,s^{-1}$). It has previously been employed in the study of SNe with strong narrow emission features such as SN 2009ip (Fraser et al. 2013, 2015), SN 2012ca (Inserra et al. 2014, 2016), and SN 2013fc (Kangas et al. 2016). Here, we also demonstrated that the fine velocity resolution allows for the measurement of narrow *absorption* features, particularly sodium absorption in SNe Ia. The higher resolution of WiFeS also frequently revealed narrow host galaxy emission features at the site of the SN, which can at times be used to determine a SN site metallicity (as we showed for SN 2012dn). Finally, the integral field nature of WiFeS allowed us to measure the local host galaxy rotational velocity at the site of several SNe, even when there was no emission directly at the SN location. Thus, WiFeS is an instrument capable of not only standard SN spectroscopic observations, but also a unique suite of capabilities not commonly found in transient follow-up instruments.

ACKNOWLEDGEMENTS

We are very grateful for the excellent technical support staff for the ANU 2.3-m telescope and the WiFeS instrument: Peter Verwayen, Ian Adams, Peter Small, Ian Price, Peter Young, and Jon Nielsen. We thank the ANU telescope time allocation committee who continue to support the observations presented herein. We also thank Julie Banfield, Michael Ireland, Stefan Keller, Lisa Kewley, Jeremy Mould, Chris Owen, Aaron Rizzuto, Dary Ruiz, and Tian-Tian Yuan for additional observations. We also thank the anonymous referee for very helpful comments.

This research was conducted by the Australian Research Council Centre of Excellence for All-sky Astrophysics (CAASTRO), through project number CE110001020. IRS was supported by Australian Research Council Laureate Grant FL0992131. This research has made use of the NASA/IPAC Extragalactic Database (NED) which is operated by the Jet Propulsion Laboratory, California Institute of Technology, under contract with the National Aeronautics and Space Administration. This research has made use of NASA's Astrophysics Data System (ADS).

REFERENCES

Aldering, G., et al. 2002, in SPIE Conf. Ser., Vol. 4836, Survey and Other Telescope Technologies and Discoveries, eds. J. A. Tyson & S. Wolff (Waikoloa: SPIE), 61, doi:10.1117/12.458107
Asplund, M., Grevesse, N., Sauval, A. J., & Scott, P. 2009, ARA&A, 47, 481
Bailey, S., et al.2009, A&A, 500, L17
Baltay, C., et al.2013, PASP, 125, 683
Barbon, R., Benetti, S., Rosino, L., Cappellaro, E., & Turatto, M. 1990, A&A, 237, 79
Benetti, S., et al.2005, ApJ, 623, 1011
Bertin, E. 2012, in ASP Conf. Ser., Vol. 461, Astronomical Data Analysis Software and Systems XXI, eds. P. Ballester, D. Egret, & N. P. F. Lorente (San Francisco: ASP), 263
Bertin, E., Mellier, Y., Radovich, M., Missonnier, G., Didelon, P., & Morin, B. 2002, in ASP Conf. Ser., Vol. 281, Astronomical Data Analysis Software and Systems XI, eds. D. A. Bohlender, D. Durand, & T. H. Handley (San Francisco: ASP), 228
Bessell, M. S. 1999, PASP, 111, 1426
Bianco, F. B., et al. 2014, ApJS, 213, 19
Blagorodnova, N., Koposov, S. E., Wyrzykowski, Ł., Irwin, M., & Walton, N. A. 2014, MNRAS, 442, 327
Blagorodnova, N., Van Velzen, S., Harrison, D. L., Koposov, S., Mattila, S., Campbell, H., Walton, N. A., & Wyrzykowski, Ł. 2016, MNRAS, 455, 603
Blondin, S., Mandel, K. S., & Kirshner, R. P. 2011, A&A, 526, A81
Blondin, S., & Tonry, J. L. 2007, ApJ, 666, 1024
Blondin, S., et al. 2012, AJ, 143, 126
Bongard, S., Baron, E., Smadja, G., Branch, D., & Hauschildt, P. H. 2006, ApJ, 647, 513
Bongard, S., Baron, E., Smadja, G., Branch, D., & Hauschildt, P. H. 2008, ApJ, 687, 456
Branch, D., Dang, L. C., & Baron, E. 2009, PASP, 121, 238
Branch, D., et al. 2006, PASP, 118, 560
Bronder, T. J., et al. 2008, A&A, 477, 717
Brown, T. M., et al. 2013, PASP, 125, 1031
Cardelli, J. A., Clayton, G. C., & Mathis, J. S. 1989, ApJ, 345, 245
Chakradhari, N. K., Sahu, D. K., Srivastav, S., & Anupama, G. C. 2014, MNRAS, 443, 1663
Childress, M., et al. 2011, ApJ, 733, 3
Childress, M. J., Filippenko, A. V., Ganeshalingam, M., & Schmidt, B. P. 2014b, MNRAS, 437, 338
Childress, M. J., Vogt, F. P. A., Nielsen, J., & Sharp, R. G. 2014a, Ap&SS, 349, 617
Childress, M. J., et al. 2015, MNRAS, 454, 3816
Cortese, L., et al. 2008, MNRAS, 383, 1519
da Costa, L. N., Pellegrini, P. S., Davis, M., Meiksin, A., Sargent, W. L. W., & Tonry, J. L. 1991, ApJS, 75, 935
Donzelli, C. J., & Pastoriza, M. G. 2000, AJ, 120, 189
Dopita, M., Hart, J., McGregor, P., Oates, P., Bloxham, G., & Jones, D. 2007, Ap&SS, 310, 255
Dopita, M., et al. 2010, Ap&SS, 327, 245
Drake, A. J., et al. 2009, ApJ, 696, 870
Filippenko, A. V. 1997, ARA&A, 35, 309
Filippenko, A. V., et al. 1992a, AJ, 104, 1543
Filippenko, A. V., et al. 1992b, ApJL, 384, L15
Folatelli, G., et al. 2013, ApJ, 773, 53
Foley, R. J., et al. 2013, ApJ, 767, 57
Fraser, M., et al. 2013, MNRAS, 433, 1312
Fraser, M., et al. 2015, MNRAS, 453, 3886
Ganeshalingam, M., et al. 2010, ApJS, 190, 418
Graur, O., Bianco, F. B., Modjaz, M., Maoz, D., Shivvers, I., Filippenko, A. V., & Li, W. 2015, preprint (arXiv:1509.08432)
Grogin, N. A., Geller, M. J., & Huchra, J. P. 1998, ApJS, 119, 277
Hachinger, S., Mazzali, P. A., & Benetti, S. 2006, MNRAS, 370, 299
Hachinger, S., Mazzali, P. A., Tanaka, M., Hillebrandt, W., & Benetti, S. 2008, MNRAS, 389, 1087

Hachinger, S., Mazzali, P. A., Taubenberger, S., Fink, M., Pakmor, R., Hillebrandt, W., & Seitenzahl, I. R. 2012, MNRAS, 427, 2057
Hatano, K., Branch, D., Lentz, E. J., Baron, E., Filippenko, A. V., & Garnavich, P. M. 2000, ApJL, 543, L49
Hicken, M., Garnavich, P. M., Prieto, J. L., Blondin, S., DePoy, D. L., Kirshner, R. P., & Parrent, J. 2007, ApJL, 669, L17
Holoien, T. W.-S., et al. 2016, MNRAS
Inserra, C., et al. 2013, ApJ, 770, 128
Inserra, C., et al. 2014, MNRAS, 437, L51
Inserra, C., et al. 2016, MNRAS, 459, 2721
Kaiser, N., et al. 2010, in Ground-based and Airborne Telescopes III, SPIE Proc. 7733, eds. L.M. Stepp, R. Gilmozzi, & H.J. Hall (San Diego: SPIE), 77330E
Kamiya, Y., Tanaka, M., Nomoto, K., Blinnikov, S. I., Sorokina, E. I., & Suzuki, T. 2012, ApJ, 756, 191
Kangas, T., et al. 2016, MNRAS, 456, 323
Keller, S. C., et al. 2007, PASA, 24, 1
Kelson, D. D. 2003, PASP, 115, 688
Kewley, L. J., & Ellison, S. L. 2008, ApJ, 681, 1183
Khan, R., Stanek, K. Z., Stoll, R., & Prieto, J. L. 2011, ApJL, 737, 24
Klotz, A., Boer, M., Atteia, J.-L., Gendre, B., Le Borgne, J.-F., Frappa, E., Vachier, F., & Berthier, J. 2013, Msngr, 151, 6
Law, N. M., et al. 2009, PASP, 121, 1395
Li, W., et al. 2011a, MNRAS, 412, 1441
Li, W., et al. 2011b, Nature, 480, 348
Lipunov, V. M., et al. 2004, AN, 325, 580
Liu, Y.-Q., Modjaz, M., Bianco, F. B., & Graur, O. 2016, ApJ, 827, 90
Maguire, K., et al. 2012, MNRAS, 426, 2359
Maguire, K., et al. 2013, MNRAS, 436, 222
Maguire, K., et al. 2014, MNRAS, 444, 3258
Matheson, T., et al. 2008, AJ, 135, 1598
Modjaz, M., et al. 2014, AJ, 147, 99
Nugent, P., Phillips, M., Baron, E., Branch, D., & Hauschildt, P. 1995, ApJL, 455, L147
Nugent, P. E., et al. 2011, Nature, 480, 344
Ogando, R. L. C., Maia, M. A. G., Pellegrini, P. S., & da Costa, L. N. 2008, AJ, 135, 2424
Oke, J. B. 1990, AJ, 99, 1621
Osterbrock, D. E., & Ferland, G. J. 2006, Astrophysics of gaseous nebulae and active galactic nuclei (Sausalito: University Science Books)
Pan, Y.-C., Sullivan, M., Maguire, K., Gal-Yam, A., Hook, I. M., Howell, D. A., Nugent, P. E., & Mazzali, P. A. 2015, MNRAS, 446, 354
Parrent, J. T., et al. 2012, ApJL, 752, L26
Parrent, J. T., et al. 2016, MNRAS, 457, 3702
Patat, F., et al. 2007, Science, 317, 924
Pereira, R., et al. 2013, A&A, 554, A27
Pettini, M., & Pagel, B. E. J. 2004, MNRAS, 348, L59
Phillips, M. M., et al. 2013, ApJ, 779, 38
Pignata, G., et al. 2009, in AIP Conf. Ser., Vol. 1111, eds. G. Giobbi, A. Tornambe, G. Raimondo, M. Limongi, L. A. Antonelli, N. Menci, & E. Brocato (Sicily: AIP), 551
Planck Collaboration et al. 2011, A&A, 536, A1
Poznanski, D., Ganeshalingam, M., Silverman, J. M., & Filippenko, A. V. 2011, MNRAS, 415, L81
Poznanski, D., Prochaska, J. X., & Bloom, J. S. 2012, MNRAS, 426, 1465
Quimby, R. M. 2006, PhD thesis, The University of Texas at Austin
Rau, A., et al. 2009, PASP, 121, 1334
Salim, S., et al. 2007, ApJS, 173, 267
Sandage, A., & Tammann, G. A. 1981, A revised Shapley-Ames Catalog of bright galaxies, Carnegie Institution of Washington Pub. 635 (Washington: Carnegie Institution)
Scalzo, R., et al. 2012, ApJ, 757, 12
Scalzo, R. A., et al. 2010, ApJ, 713, 1073
Shappee, B. J., et al. 2014, ApJ, 788, 48
Silverman, J. M., Ganeshalingam, M., Li, W., Filippenko, A. V., Miller, A. A., & Poznanski, D. 2011, MNRAS, 410, 585
Silverman, J. M., Ganeshalingam, M., Li, W., & Filippenko, A. V. 2012a, MNRAS, 425, 1889
Silverman, J. M., Kong, J. J., & Filippenko, A. V. 2012b, MNRAS, 425, 1819
Silverman, J. M., Vinkó, J., Marion, G. H., Wheeler, J. C., Barna, B., Szalai, T., Mulligan, B. W., & Filippenko, A. V. 2015, MNRAS, 451, 1973
Silverman, J. M., et al. 2012c, MNRAS, 425, 1789
Simon, J. D., et al. 2009, ApJ, 702, 1157
Smartt, S. J., et al. 2015, A&A, 579, A40
Sternberg, A., et al. 2011, Science, 333, 856
Sternberg, A., et al. 2014, MNRAS, 443, 1849
Stritzinger, M., Suntzeff, N. B., Hamuy, M., Challis, P., Demarco, R., Germany, L., & Soderberg, A. M. 2005, PASP, 117, 810
Tanaka, M., et al. 2010, ApJ, 714, 1209
Taubenberger, S., et al. 2011, MNRAS, 412, 2735
Taubenberger, S., et al. 2013, MNRAS, 432, 3117
Theureau, G., Bottinelli, L., Coudreau-Durand, N., Gouguenheim, L., Hallet, N., Loulergue, M., Paturel, G., & Teerikorpi, P. 1998a, A&AS, 130, 333
Theureau, G., Bottinelli, L., Coudreau-Durand, N., Gouguenheim, L., Hallet, N., Loulergue, M., Paturel, G., & Teerikorpi, P. 1998b, A&AS, 130, 333
Tomasella, L., et al. 2014, AN, 335, 841
Tremonti, C. A., et al. 2004, ApJ, 613, 898
Turatto, M., Benetti, S., & Cappellaro, E. 2003, in From Twilight to Highlight: The Physics of Supernovae, Proc. of the ESO/MPA/MPE Workshop, eds. W. Hillebrandt & B. Leibundgut (Garching: ESO), 200
van Dokkum, P. G. 2001, PASP, 113, 1420
Wang, X., et al. 2009, ApJL, 699, L139
Wyrzykowski, L., Hodgkin, S., Blogorodnova, N., Koposov, S., & Burgon, R. 2012, preprint (arXiv:1210.5007)
Wyrzykowski, Ł., et al. 2014, ACTA, 64, 197
Yamanaka, M., et al. 2009, ApJL, 707, L118
Yaron, O., & Gal-Yam, A. 2012, PASP, 124, 668
York, D. G., et al. 2000, AJ, 120, 1579
Yuan, F. 2010, PhD thesis, University of Michigan
Yuan, F., et al. 2010, ApJ, 715, 1338
Zhao, X., et al. 2015, ApJS, 220, 20

APPENDIX A1: TARGET AND OBSERVATION DETAILS

In this Appendix, we present the observational metadata for the AWSNAP data release, as well as sodium fit results and host (or local) redshifts used in the sodium fitting.

AWSNAP targets: Table A1 presents the discovery and classification details for the full list of 175 objects featured in the AWSNAP

Table A1. All AWSNAP Targets.

	Discovery					Classification					
SN	RA	DEC	Ref.[a]	Date	Group[b]	Ref.	Date	Group[c]	SN type	Redshift	Phase[d]
SN 2009ip	22:23:08.1	−28:56:35	A4334	20120724	CRTS	A4338	20120826	Foley	SNIIn	0.005944	(unk)
SN 2012ca	18:41:06.5	−41:47:38	C3101	20120426	Parker	A4076	20120429	PESSTO	SNIIn	0.019000	(unk)
SN 2012dj	23:14:47.2	−43:36:22	C3167	20120702	Parker	C3167	20120706	Parrent	SNIb/c	0.005324	+0
SN 2012dn	20:23:36.3	−28:16:43	C3174	20120708	Parker	A4253	20120712	SNF	SNIa	0.010187	−10
SN 2012dt	00:56:38.1	-09:53:59	C3188	20120718	Parker	A4269	20120721	PTF	SNII	0.018900	+9
SN 2012dy	21:18:49.5	−57:38:42	C3197	20120804	Bock	C3197	20120805	Milisavljevic	SNII	0.010300	(young)
SN 2012ec	02:45:59.9	−07:34:15	C3201	20120811	Monard	A4306	20120812	AWSNAP	SNII	0.004693	(young)
SN 2012eq	01:00:14.5	−30:48:26	C3223	20120827	CRTS	A4362	20120907	PESSTO	SNIa	0.032230	+45
SN 2012eu	03:13:04.2	−08:23:24	C3231	20120827	CRTS	C3231	20120904	Yang	SNIa	0.030000	+30
SN 2012fr	03:33:37.1	−36:07:28	A4523	20121027	TAROT	A4525	20121028	AWSNAP	SNIa	0.005400	−11
SN 2012hr	06:21:37.7	−59:42:39	C3346	20121216	Marples	A4663	20121220	Morrell	SNIa	0.008000	−8
SN 2013K	17:39:33.1	−85:18:18	C3391	20130120	Parker	A4754	20130121	PESSTO	SNII	0.008000	+2
SN 2013aa	14:32:33.3	−44:13:20	C3416	20130213	Parker	A4817	20130213	LCOGT	SNIa	0.003999	−3
SN 2013ai	06:16:18.4	−21:22:23	C3431	20130226	Conseil	A4851	20130302	PESSTO	SNII	0.009000	+0
SN 2013aj	13:54:00.8	−07:55:37	C3434	20130303	Contini	A4852	20130303	PESSTO	SNIa	0.009000	−7
SN 2013am	11:18:56.3	+13:03:56	C3440	20130321	Sugano	A4909	20130322	ASP	SNII	0.002692	(young)
SN 2013ao	11:44:44.7	−20:31:41	C3442	20130304	CRTS	A4863	20130305	PESSTO	SNIa	0.030000	−7
SN 2013bj	14:04:19.9	−07:03:02	C3482	20130404	ISSP	A4975	20130412	AWSNAP	SNII	0.030000	+44
SN 2013bk	09:40:47.6	−05:26:07	C3483	20130407	CRTS	A4975	20130412	AWSNAP	SNIc	0.020000	+3
SN 2013by	16:59:01.5	−60:11:22	C3506	20130423	Parker	C3506	20130424	Morrell	SNII	0.003816	(young)
SN 2013bz	13:26:50.7	−10:01:39	C3507	20130421	CRTS	C3507	20130430	Chen	SNIa-SC	0.015000	+0
SN 2013cg	09:26:57.3	−24:47:01	C3517	20130506	CHASE	A5057	20130508	LCOGT	SNIa	0.007952	−7
SN 2013cs	13:15:14.2	−17:57:56	C3533	20130512	LSQ	A5067	20130514	LSQ	SNIa	0.009240	−7
SN 2013cy	22:10:33.5	−22:39:48	C3546	20130531	Monard/LSQ	A5100	20130603	AWSNAP	SNIa	0.034000	+0
SN 2013cz	19:49:32.5	−70:12:59	C3547	20130507	Parker	A5101	20130603	AWSNAP	SNII	0.015000	+21
SN 2013df	12:26:28.1	+31:13:50	C3557	20130607	ISSP	C3557	20130610	Cenko	SNIIb	0.002388	(young)
SN 2013dh	15:30:00.3	+12:59:27	C3561	20130612	LOSS	C3561	20130614	Cenko	SNIa-91T	0.013356	−5
SN 2013du	01:24:13.6	−34:43:27	C3579	20130623	Parker	A5194	20130704	AWSNAP	SNII	0.019000	+30
SN 2013ef	01:55:20.2	+06:36:35	A5193	20130704	ASAS-SN	A5194	20130704	AWSNAP	SNIa	0.015000	+0
SN 2013ej	01:36:48.2	+15:45:35	C3606	20130725	LOSS	A5228	20130727	LCOGT	SNII	0.002192	(young)
SN 2013ek	20:57:54.2	−51:52:10	C3607	20130724	Parker	A5227	20130725	LCOGT	SNIb	0.016000	+5
SN 2013er	13:07:51.2	−00:51:54	C3619	20130729	Parker	A5238	20130731	AWSNAP	SNIa	0.018052	-4
SN 2013fd	01:33:59.6	−34:23:38	C3645	20130827	Parker	A5345	20130829	PESSTO	SNII	0.013000	(young)
SN 2013fj	22:15:28.3	+15:34:06	C3654	20130907	ISSP	C3654	20130913	ASP	SNIa	0.033570	+4
SN 2013fq	19:59:06.7	−55:55:36	C3665	20130915	Parker	A5400	20130918	Hsiao	SNIIb	0.011300	+0
SN 2013fs	23:19:44.5	+10:10:38	C3671	20131006	Itagaki	A5527	20131008	AWSNAP	SNII	0.012000	(young)
SN 2013ft	23:41:36.9	+03:43:16	C3672	20130913	LOSS	A5455	20131008	AWSNAP	SNII	0.009600	+13
SN 2013fw	21:13:44.1	+13:34:50	C3681	20131022	Jin,Gao	A5507	20131024	LCOGT	SNIa	0.016952	−14
SN 2013gh	22:02:21.8	−18:55:00	C3706	20130808	LOSS	A5262	20130811	LCOGT	SNIa	0.008800	−7
SN 2013gi	06:23:48.2	−65:19:43	C3714	20131113	Parker	A5582	20131114	AWSNAP	SNIa	0.030100	+10
SN 2013gq	19:59:07.8	−55:55:03	C3730	20130325	LOSS	A4940	20130402	PESSTO	SNIa	0.014000	+0
SN 2013gr	01:46:28.5	−58:40:25	C3733	20131128	Marples	A5612	20131130	Hsiao	SNIax	0.007000	+0
SN 2013hh	11:29:04.8	+17:14:08	C3754	20131111	TAROT	A5656	20131212	AWSNAP	SNIa-91T	0.012000	−2
SN 2013hj	09:12:05.7	−15:25:39	C3757	20131212	CHASE	C3757	20131213	ASP	SNII	0.006900	(young)

PASA, 33, e055 (2016)
doi:10.1017/pasa.2016.47

Table A1. Continued.

	Discovery					Classification					
SN	RA	DEC	Ref.[a]	Date	Group[b]	Ref.	Date	Group[c]	SN type	Redshift	Phase[d]
SN 2013hn	13:50:52.3	−30:16:54	C3762	20131213	Kot+	C3762	20131217	LCOGT	SNIa	0.015140	−5
SN 2013hu	11:28:07.2	−13:11:24	C3776	20131228	Itagaki	A5716	20140101	PESSTO	SNII	0.015000	+25
SN 2013hx	01:35:33.4	−57:57:55	C3836	20131227	SkyMapper	A5912	20140220	PESSTO	SLSN	0.135000	+0
SN 2014D	12:10:37.1	+18:49:50	C3778	20140101	CRTS	A5742	20140109	ASP	SNIa	0.008179	−2
SN 2014E	12:03:31.9	+02:02:46	C3784	20140105	PTF	A5741	20140106	PTF	SNIa	0.018906	−3
SN 2014I	05:42:20.1	−25:32:34	C3791	20140117	Parker	A5777	20140118	AWSNAP	SNIa	0.030014	−1
SN 2014L	12:18:48.3	+14:24:55	C3795	20140126	TNTS	C3795	20140127	TNTS	SNIc	0.008029	+0
SN 2014N	02:30:59.0	−44:25:26	C3798	20140127	Parker	C3798	20140202	Drout	SNII	0.017000	+35
SN 2014X	12:10:41.3	−34:03:28	C3820	20140301	Parker	A5948	20140304	AWSNAP	SNIa	0.021000	+21
SN 2014aa	11:45:03.3	+19:58:38	C3823	20140307	Arbor	A5958	20140309	ASP	SNIa	0.016982	−7
SN 2014ac	15:04:39.7	+12:38:02	C3830	20140310	ISSP	A5970	20140310	PESSTO	SNIa	0.030000	+0
SN 2014ad	11:57:44.0	−10:10:03	C3831	20140312	CRTS	C3831	20140315	Jha	SNIc-BL	0.005700	(young)
SN 2014ah	11:55:30.4	+11:55:28	C3835	20140312	ISSP	C3835	20140311	ASP	SNIa	0.021026	−7
SN 2014ao	08:34:33.2	−02:32:33	C3855	20140417	LOSS	A6077	20140417	ASP	SNIa	0.014000	−10
SN 2014ap	11:30:13.3	+24:10:17	C3856	20140320	ISSP	A6001	20140322	AWSNAP	SNIa	0.023516	−1
SN 2014at	21:46:13.9	−46:31:21	C3862	20140420	Parker	A6087	20140420	PESSTO	SNIa	0.030000	−7
SN 2014au	14:19:29.6	−05:37:29	C3864	20140420	CRTS	A6091	20140422	PESSTO	SNII	0.034920	+16
SN 2014bx	19:43:52.4	−70:37:52	C3926	20140720	Parker	A6335	20140722	AWSNAP	SNIa	0.011570	−1
SN 2014bz	13:56:04.2	−43:35:10	C3932	20140506	Conseil	A6230	20140611	AWSNAP	SNIa	0.022516	+30
SN 2014ca	16:53:20.9	−72:30:52	C3935	20140510	Parker	A6230	20140611	AWSNAP	SNII	0.019487	+65
SN 2014cm	18:08:30.6	−52:04:11	C3951	20140530	Parker	A6230	20140611	AWSNAP	SNII	0.018219	+71
SN 2014co	01:10:35.5	−30:13:33	C3953	20140621	Monard	A6302	20140708	AWSNAP	SNII	0.019036	+10
SN 2014cp	02:25:29.7	−25:37:36	C3954	20140623	Parker	A6302	20140708	AWSNAP	SNIc-BL	0.016164	+1
SN 2014cq	09:23:29.6	−63:40:28	C3955	20140620	Parker	A6302	20140708	AWSNAP	SNIIb	0.010673	+20
SN 2014cr	19:37:05.5	−42:17:44	C3956	20140627	Monard	A6302	20140708	AWSNAP	SNIax	0.019123	+23
SN 2014cs	21:35:51.9	−62:05:33	C3957	20140622	Parker	A6302	20140708	AWSNAP	SNIa	0.053664	+23
SN 2014ct	09:59:25.2	−00:15:19	C3958	20140601	Parker	A6230	20140611	AWSNAP	SNIa	0.047987	+24
SN 2014cu	21:50:47.1	−73:55:27	C3959	20140622	Parker	A6302	20140708	AWSNAP	SNII	0.028326	+20
SN 2014cw	22:15:26.7	−10:28:40	C3962	20140829	MASTER	A6440	20140902	PESSTO	SNII	0.006000	+0
SN 2014cx	00:59:47.9	−07:34:26	C3963	20140902	Itagaki	A6440	20140902	PESSTO	SNII	0.005490	(young)
SN 2014cy	23:44:16.1	+10:46:05	C3964	20140831	Nishimura	A6437	20140902	LCOGT	SNII	0.005547	(young)
SN 2014dc	03:30:54.6	−47:58:49	C3970	20140904	Maza	C3970	20140910	Beletsky/AWSNAP	SNII	0.022436	−2
SN 2014df	03:44:24.5	−44:40:04	C3977	20140603	Monard	A6201	20140603	AWSNAP	SNIb	0.003896	+6
SN 2014dl	16:29:46.1	+08:38:31	C3995	20140925	CRTS	A6507	20140926	ASP	SNIa-91T	0.032966	−6
SN 2014dn	04:17:54.8	−56:36:48	C3997	20140924	Parker	A6510	20140928	Morrell	SNIa-pec	0.022189	+3
SN 2014do	08:17:47.8	−30:07:25	C4000	20140928	Parker	A6536	20141003	AWSNAP	SNII	0.005520	+13
SN 2014dp	08:19:38.2	−22:34:17	C4002	20140928	Parker	A6562	20141009	AWSNAP	SNIb	0.018951	+11
SN 2014dq	22:23:16.4	−28:58:34	A6592	20141019	ASAS-SN	A6600	20141020	Challis	SNII	0.006000	(young)
SN 2014dr	03:22:46.6	+00:09:28	C4009	20141014	CRTS	A6610	20141023	ASP	SNII	0.023000	+45
SN 2014eg	02:45:09.0	−55:44:27	A6711	20141116	PESSTO	A6739	20141122	PESSTO	SNIa-91T	0.018000	−7
SN 2015F	07:36:16.3	−69:30:17	C4081	20150309	Monard	A7209	20150310	PESSTO	SNIa	0.004000	−11
SN 2015J	07:35:07.0	−69:08:01	C4115	20150427	SkyMapper	A7711	20150624	AWSNAP	SNIIn	0.005400	(unk)
SN 2015L	22:02:14.3	−61:39:32	A7642	20150614	ASAS-SN	A7774	20150621	Dong	SLSN	0.232600	(unk)
SN 2015S	00:31:26.7	−49:35:35	C4130	20150722	Marples	A7866	20150731	AWSNAP	SNII	0.021912	+2

PASA, 33, e055 (2016)
doi:10.1017/pasa.2016.47

Table A1. Continued.

	Discovery					Classification					
SN	RA	DEC	Ref.[a]	Date	Group[b]	Ref.	Date	Group[c]	SN type	Redshift	Phase[d]
ASASSN-13co	21:40:38.5	+06:30:40	A5346	20130829	ASAS-SN	A5353	20130901	Morrell	SNII	0.022600	+0
ASASSN-14dp	11:21:58.4	−37:54:25	A6297	20140707	ASAS-SN	A6302	20140708	AWSNAP	SNII	0.009159	−1
ASASSN-14eu	15:00:36.9	−03:50:52	A6360	20140801	ASAS-SN	A6363	20140802	Milisavljevic	SNIa	0.022722	+0
ASASSN-14ew	20:22:00.7	−51:47:48	A6367	20140804	ASAS-SN	A6384	20140811	Takats	SNIa	0.019597	+0
ASASSN-14fo	20:34:06.5	−01:58:13	A6397	20140815	ASAS-SN	A6399	20140816	PESSTO	SNIa	0.020000	+2
ASASSN-14fw	23:49:06.7	−07:03:05	A6404	20140818	ASAS-SN	A6417	20140824	PESSTO	SNIa	0.019000	+10
ASASSN-14ha	04:20:02.0	−54:56:19	A6460	20140910	ASAS-SN	A6466	20140913	LCOGT	SNII	0.005017	(young)
ASASSN-14hr	01:50:41.6	−14:31:08	A6500	20140925	ASAS-SN	A6508	20140927	CSP	SNIa	0.033620	−5
ASASSN-14hu	06:43:27.5	−69:38:17	A6505	20140927	ASAS-SN	A6510	20140928	CSP	SNIa	0.015000	−5
ASASSN-14ig	01:16:05.3	−61:37:21	A6517	20140921	ASAS-SN	A6536	20141003	AWSNAP	SNIa	0.030000	+15
ASASSN-14ih	22:34:30.4	−24:39:54	A6521	20140919	ASAS-SN	A6536	20141003	AWSNAP	SNIa	0.032000	+20
ASASSN-14ii	22:16:41.5	−36:09:42	A6521	20140922	ASAS-SN	A6536	20141003	AWSNAP	SNIa	0.030000	+9
ASASSN-14il	00:45:33.0	−14:15:34	A6525	20141001	ASAS-SN	A6536	20141003	AWSNAP	SNIIn	0.022000	(young)
ASASSN-14jc	07:35:34.7	−62:46:10	A6594	20141019	ASAS-SN	A6618	20141023	PESSTO	SNIa	0.011320	+0
ASASSN-14jg	23:33:14.5	−60:34:13	A6637	20141021	ASAS-SN	A6661	20141102	LCOGT	SNIa	0.014800	+0
ASASSN-14ko	05:25:16.5	−45:59:24	A6732	20141114	ASAS-SN	A6749	20141124	PESSTO	SNIIn	0.042000	(unk)
ASASSN-14kp	00:39:38.6	−38:04:38	A6736	20141122	ASAS-SN	A6765	20141127	CSP	SNII	0.023000	+0
ASASSN-14kq	23:45:15.5	−29:47:01	A6737	20141123	ASAS-SN	A6765	20141127	CSP	SNIa	0.034000	−2
ASASSN-14lp	12:45:08.6	−00:27:29	A6795	20141210	ASAS-SN	A6801	20141211	Thorstensen	SNIa	0.005101	−3
ASASSN-14lt	03:11:07.4	−13:06:30	A6802	20141210	ASAS-SN	A6804	20141212	ASP	SNIa	0.032000	−7
ASASSN-14lw	01:06:47.6	−46:58:55	A6809	20141212	ASAS-SN	A6832	20141216	AWSNAP	SNIa-91T	0.016000	−4
ASASSN-15aj	10:52:54.2	−32:55:26	A6886	20150108	ASAS-SN	A6905	20150112	Simon	SNIa	0.010921	+1
ASASSN-15al	04:57:49.6	−21:35:35	A6894	20150104	ASAS-SN	A6909	20150112	PESSTO	SNIa	0.030000	+0
ASASSN-15as	09:39:16.8	+06:25:56	A6919	20150113	ASAS-SN	A6920	20150114	Morrell	SNIa	0.030000	+0
ASASSN-15az	11:08:38.0	−10:14:48	A6921	20150114	ASAS-SN	A6925	20150115	ASP	SNIa	0.028000	+0
ASASSN-15ba	14:04:55.1	+08:55:15	A6934	20150115	ASAS-SN	A6947	20150115	Challis	SNIa	0.023100	−5
ASASSN-15dz	16:41:20.9	+08:54:32	A7145	20150221	ASAS-SN	A7180	20150306	AWSNAP	SNIa	0.032216	+9
ASASSN-15eb	08:06:07.8	−22:33:51	A7157	20150226	ASAS-SN	A7180	20150306	AWSNAP	SNIa	0.016481	+8
ASASSN-15go	06:11:22.5	−16:25:21	A7349	20150406	ASAS-SN	A7368	20150411	AWSNAP	SNIa	0.018923	−4
ASASSN-15hs	15:33:34.7	−78:07:12	A7444	20150424	ASAS-SN	A7458	20150429	AWSNAP	SNIIn	0.008900	(unk)
ASASSN-15hx	13:43:16.7	−31:33:21	A7447	20150426	ASAS-SN	A7452	20150426	PESSTO	SNIa	0.010000	−11
ASASSN-15hy	20:10:01.6	−00:44:16	A7450	20150425	ASAS-SN	A7452	20150426	PESSTO	SNIa-pec	0.025000	−13
ASASSN-15hz	22:29:37.8	−65:27:44	A7450	20150426	ASAS-SN	A7458	20150429	AWSNAP	SNIa	0.033000	−3
ASASSN-15ic	06:14:52.0	−42:48:00	A7455	20150427	ASAS-SN	A7458	20150429	AWSNAP	SNIa	0.025000	−1
ASASSN-15lv	01:59:01.0	−32:22:28	A7700	20150705	ASAS-SN	A7746	20150701	AWSNAP	SNIIb	0.011000	−2
SNhunt222	10:00:26.2	+03:22:50	CTOCP	20131214	CRTS/LSQ	A5860	20140207	PESSTO	SNII	0.006860	+60
SNhunt239	12:09:09.7	+31:34:28	CTOCP	20140325	CRTS	A6040	20140402	AWSNAP	SNIa-91bg	0.022666	+10
SNhunt259	00:00:21.6	−02:36:23	CTOCP	20141015	CRTS	(NEW)	20141018	AWSNAP	SNIa	0.037909	+100
SNhunt261	02:45:29.8	−17:31:41	CTOCP	20141017	CRTS	A6629	20141027	AWSNAP	SNIa-91bg	0.029070	+2
CSS1222	12:22:57.0	+28:29:57	CRTS	20140326	CRTS	A6040	20140402	AWSNAP	SNII	0.024000	+2
Gaia15agm	23:55:57.6	−43:43:40	Gaia	20150601	Gaia	A7746	20150701	AWSNAP	SNIa	0.029000	+31
LSQ12dlf	01:50:29.8	−21:48:45	LSQ	20120710	LSQ	A4329	20120818	PESSTO	SLSN-Ic	0.250000	+21
LSQ12ege	16:50:51.7	+02:52:40	LSQ	20120715	LSQ	A4303	20120809	PESSTO	SNIa	0.080000	−5
LSQ12ehh	16:27:12.4	+02:05:12	LSQ	20120727	LSQ	A4303	20120809	PESSTO	SNIa	0.100000	−6
LSQ12ers	23:02:03.3	−22:52:17	LSQ	20120829	LSQ	A4357	20120906	AWSNAP	SNIa	0.099000	+1

PASA, 33, e055 (2016)
doi:10.1017/pasa.2016.47

PASA, 33, e055 (2016)
doi:10.1017/pasa.2016.47

Table A1. Continued.

	Discovery					Classification					
SN	RA	DEC	Ref.[a]	Date	Group[b]	Ref.	Date	Group[c]	SN type	Redshift	Phase[d]
LSQ12euu	21:31:07.5	−06:41:49	LSQ	20120902	LSQ	A4357	20120906	AWSNAP	SNIa	0.116000	−1
LSQ12eve	21:53:16.7	−21:42:45	LSQ	20120903	LSQ	A4357	20120906	AWSNAP	SNIa	0.098000	−7
LSQ12gdj	23:54:45.3	−25:40:36	LSQ	20121107	LSQ	A4566	20121110	SNF	SNIa-91T	0.030324	−5
LSQ13ddu	03:58:48.4	−29:24:54	LSQ	20131122	LSQ	–	20131130	PESSTO	SLSN	0.058000	(unk)
LSQ13pp	12:42:02.9	−22:05:07	LSQ	20130318	LSQ	(NEW)	20130325	AWSNAP	SNII	0.045700	+7
LSQ14bcj	14:05:58.2	−12:04:12	LSQ	20140403	LSQ	A6087	20140420	PESSTO	SNIa	0.020000	−7
LSQ15adm	20:14:20.9	−58:08:01	LSQ	20150405	LSQ	A7363	20150409	PESSTO	SNIa-csm	0.073000	+10
LSQ15ey	14:12:05.1	−07:23:37	LSQ	20150120	LSQ	A6994	20150125	PESSTO	SNII	0.036000	(young)
MASTERJ1408	14:08:04.9	−11:59:46	A6084	20140330	MASTER	A6092	20140423	AWSNAP	SNIa	0.035308	+25
MASTERJ1353	13:53:30.3	−42:16:19	A7151	20150227	MASTER	A7209	20150310	PESSTO	SNIIn	0.052000	+10
MASTERJ0746	07:46:10.7	−71:22:20	A7451	20150426	MASTER	A7458	20150429	AWSNAP	SNIa	0.017400	−7
OGLE-2013-SN-070	00:45:15.0	−66:19:06	A5397	20130910	OGLE	A5455	20131008	AWSNAP	SNIa	0.043000	+33
OGLE-2014-SN-019	06:13:50.4	−67:55:13	A5916	20140222	OGLE	A5915	20140222	PESSTO	SNIa	0.040000	−3
OGLE-2014-SN-021	05:48:25.3	−66:47:31	A5916	20140224	OGLE	A5919	20140224	AWSNAP	SNIa	0.039000	+0
OGLE-2014-SN-067	04:57:50.4	−74:00:40	A6423	20140815	OGLE	A6430	20140829	AWSNAP	SNIc	0.018700	+0
PS1-14lz	04:50:48.8	−14:25:23	PS1	20140213	PanSTARRS	A5908	20140219	PESSTO	SNIa	0.070000	+1
PS1-14md	11:17:42.3	−21:14:35	PS1	20140213	PanSTARRS	A5919	20140224	AWSNAP	SNIa	0.071000	+3
PS1-14ra	14:41:28.3	+09:26:12	PS1	20140305	PanSTARRS	A5957	20140307	PESSTO	SNIa	0.030000	+0
PS1-14vw	09:58:07.5	+07:57:57	PS1	20140325	PanSTARRS	A6040	20140402	AWSNAP	SNIa	0.091000	+14
PS1-14vx	10:41:50.9	+16:49:06	PS1	20140325	PanSTARRS	A6040	20140402	AWSNAP	SNIa	0.057000	+23
PS1-14wl	13:32:42.0	−20:36:24	PS1	20140325	PanSTARRS	A6040	20140402	AWSNAP	SNIa	0.034000	+0
PS15ae	11:33:41.7	+00:43:40	PS1	20141223	CRTS/PS1	A7102	20150217	PESSTO	SLSN-Ic	0.110000	+0
PS15br	11:25:19.2	+08:14:18	PS1	20150215	PanSTARRS	A7209	20150310	PESSTO	SLSN	0.101000	(unk)

https://doi.org/10.1017/pasa.2016.47 Published online by Cambridge University Press

PASA, 33, e055 (2016)
doi:10.1017/pasa.2016.47

Table A1. Continued.

	Discovery					Classification					
SN	RA	DEC	Ref.[a]	Date	Group[b]	Ref.	Date	Group[c]	SN type	Redshift	Phase[d]
PSNJ02454138-0812301	02:45:41.4	−08:12:30	CTOCP	20141024	ISSP	A6628	20141027	ASP	SNIa	0.029613	+3
PSNJ05031639-0256110	05:03:16.4	−02:56:11	CTOCP	20141105	LOSS	A6682	20141110	Kangas	SNIb	0.014440	+0
PSNJ09023787+2556042	09:02:37.9	+25:56:04	A7366	20150411	LOSS	A7368	20150411	AWSNAP	SNIIb	0.008172	−3
PSNJ09204691-0803340	09:20:46.9	−08:03:34	CTOCP	20141120	Gagliano	A6734	20141121	NAOC	SNIIn	0.019644	−10
PSNJ10433393-3048206	10:43:33.9	−30:48:21	CTOCP	20150211	Parker	A7073	20150212	Morrell	SNIIn	0.013000	+117
PSNJ11484578-2817312	11:48:45.8	−28:17:31	CTOCP	20131127	CHASE	A5615	20131129	PESSTO	SNIc-BL	0.010000	+20
PSNJ13471211-2422171	13:47:12.1	−24:22:17	CTOCP	20150212	Parker	A7075	20150215	Stritzinger	SNIa	0.019910	+0
PSNJ17194328-7721305	17:19:43.3	−77:21:31	CTOCP	20130825	Aldous	A5331	20130826	PESSTO	SNIa	0.009000	−4
PSNJ17285509-6609103	17:28:55.1	−66:09:10	CTOCP	20130827	Marples	A5338	20130828	PESSTO	SNII	0.021908	+7
PSNJ19251269-5336028	19:25:12.7	−53:36:03	CTOCP	20150810	Parker	A7925	20150817	AWSNAP	SNIa	0.054000	+48
PSNJ20250386-2449133	20:25:04.1	−24:49:20	A6659	20141028	LOSS	A6667	20141104	LCOGT	SNIc	0.010614	−3
PSNJ23320218-4545032	23:32:02.2	−45:45:03	CTOCP	20120828	CRTS	(NEW)	20120907	AWSNAP	SNIc	0.005000	+60
PTF12gzk	22:12:41.5	+00:30:53	A4298	20120724	PTF	A4298	20120727	PTF	SNIc-BL	0.013700	(young)
iPTF13bvn	14:59:59.4	+01:52:59	A5147	20130616	iPTF	A5142	20140617	Milisavljevic	SNIb	0.004490	−32
iPTF13dge	05:03:35.3	+01:34:15	A5366	20130904	iPTF	A5366	20130904	PTF	SNIa	0.015854	−15
SMTJ10310056-3658262	10:30:40.0	−36:57:51	A7261	20150313	SkyMapper	A7261	20150319	PESSTO	SNIa	0.035000	+0
SMTJ03253351-5344190	03:25:33.8	−53:44:22	A5641	20131201	SkyMapper	A5641	20131206	AWSNAP	SNIa	0.055000	−6
SMTJ05451320-4735425	05:45:13.7	−47:35:37	–	20150315	SkyMapper	–	–	LCOGT	SNIa	0.050000	+0
SMTJ13494831-0658174	13:49:48.0	−06:58:17	A7925	20150728	SkyMapper	A7925	20150817	AWSNAP	SNIa	0.076933	+12

[a] Notation: A1234 ≡ ATel # 1234; C1234 ≡ CBET # 1234; CTOCP ≡ CBET Transient Object Confirmation Page; objects newly classified here denoted as (NEW); all others refer to transient announcement webpages for stated discovery group(s).
[b] Discovery group acronyms (where appropriate—see text for details) or lead author of the discovery alert.
[c] Classifcation group acronyms (where appropriate—see text for details) or lead author of the classification alert.
[d] Phase with respect to maximum light (where appropriate) for the best *spectroscopic match*, as reported by the classifying group. SNe IIn do not typically have a clearly identifiable spectroscopic phase so are listed as '(unk)' (i.e. unknown). Very young SNe II (with very blue featureless continua) similarly have ambiguous phases so are listed as '(young)'.

DR1 data release. We list the discovery location and date, as well as discovery reference and group that discovered the transient. Note the discovery references are typically either Astronomer's Telegrams (ATel's, denoted as, e.g. 'A1234') or telegrams from the Central Bureau for Electronic Telegrams (CBET's, denoted as, e.g. 'C1234'), though occasionally a separate discovery notice was not issued—in these cases, typically the webpage of the discovering group was cited in the classification reference. Classification references are given with similar notation, listed along with classification date, quoted supernova type and phase from the classification, as well as the redshift listed in the classification.

In Table A1, the discovery and classification groups are listed either as acronyms of the group name, or listed as the first author in the discovery/classification notice. The acronyms used in the table for discovery groups are as follows:

- ASAS-SN: the All-Sky Automated Survey for Supernovae (Shappee et al. 2014).
- CHASE: the CHilean Automatic Supernova sEarch (Pignata et al. 2009).
- CRTS: the Catalina Real-Time Transient Survey (Drake et al. 2009).
- Gaia: transient alerts from Gaia (e.g. Wyrzykowski et al. 2012; Blagorodnova et al. 2014, 2016).
- ISSP: the Italian Supernova Search Programme.
- LOSS: the Lick Observatory Supernova Search (Ganeshalingam et al. 2010).
- LSQ: the La Silla-QUEST low redshift supernova survey (Baltay et al. 2013).
- MASTER: the Mobile Astronomical System of Telescope-Robots (Lipunov et al. 2004).
- OGLE: the OGLE-IV real-time transient search (Wyrzykowski et al. 2014).
- PanSTARRS: the Panoramic Survey Telescope and Rapid Response System panstarrs.
- PTF/iPTF: the Palomar Transient Factory (Rau et al. 2009; Law et al. 2009) and its successor.
- SkyMapper: the SkyMapper (Keller et al. 2007) transients search.
- TAROT: the Télescope á Action Rapide pour les Objets Transitoires (Rapid Action Telescope for Transient Objects) at La Silla (e.g. Klotz et al. 2013).
- TNTS: the Tsinghua-NAOC Transient Survey.

The acronyms used in the table for classification groups are as follows:

- ASP: the Asiago Supernova Programme (Tomasella et al. 2014).
- AWSNAP: the ANU+WiFeS SuperNovA Programme (this work).
- CSP: the Carnegie Supernova Project (Folatelli et al. 2013).
- LCOGT: the Las Cumbres Observatory Global Telescope (Brown et al. 2013).
- PESSTO: the Public ESO Spectroscopic Survey for Transient Objects (Smartt et al. 2015).
- SNF: SuperNova Factory (Aldering et al. 2002).

Some transients in Table A1 are known by other aliases or are listed in shorthand form (due to a lengthy full name). These transients and their aliases (or full names) are noted in Table A2.

Table A2. Alternate and/or full designations for SNe in the AWSNAP sample.

SN	Alias
SN 2013ef	ASASSN-13bb
SN 2014E	PTF14w
SN 2014cx	ASASSN-14gm
SN 2014dq	ASASSN-14jb
SN 2015L	ASASSN-15lh
iPTF13dge	PS1-13dvn
LSQ15adm	Gaia15aep
LSQ15ey	PS15ii
PS15ae	CSS141223:113342+004332
PSNJ09023787+2556042	Gaia15aet
PSNJ10433393-3048206	PS15ip
PSNJ20250386-2449133	PS15bjv
SNhunt222	LSQ14rl
CSS1222	PS1-14ya
CSS1222	CSS140326:122257+282955
MASTERJ1408	MASTER OT J140804.26-115949.7
MASTERJ1353	MASTER OT J135329.90-421622.5
MASTERJ0746	MASTER OT J074610.09-712224.9

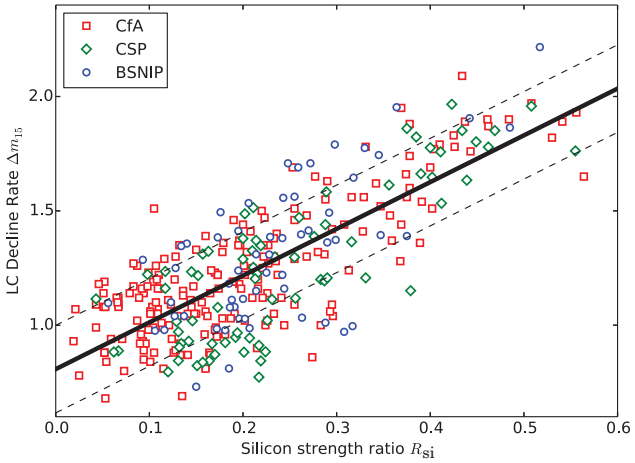

Figure A1. Literature data used to fit the trend of Δm_{15} versus $R_{\rm Si}$. The best fit is the thick solid line, and the thin dashed line represent the trend $\pm 1\sigma$ (where σ is the dispersion of the data about the trend).

AWSNAP spectra: The full list of AWSNAP spectra released here is given in Table A3, along with pertinent observation details such as grating and exposure time.

SN Ia sodium fits: In Table A4, we present the best fit parameters (and uncertainties) for our fits to narrow sodium absorption in our sample of SN Ia maximum light spectra. Table A5 lists the redshifts used to establish the local rest velocity of the SN—typically this was the redshift of the host galaxy but occasionally is obtained from galaxy emission features at the location of the SN (denoted as 'Local').

APPENDIX A2: DERIVATION OF THE SN Ia $R_{\rm Si}$–Δm_{15} RELATION FROM LITERATURE DATA

Our fit to the relation between Δm_{15} and $R_{\rm Si}$ is presented here. Our fit to the data is shown in Figure A1, and from these data we derive

Table A3. All AWSNAP spectra.

SN	Observation date	Grating	Exposure time (s)
SN 2009ip	2012-Oct-22	B3000	1 200
SN 2009ip	2012-Oct-22	R3000	1 200
SN 2009ip	2012-Oct-23	B7000	1 200
SN 2009ip	2012-Oct-23	R7000	1 200
SN 2009ip	2012-Sep-22	B3000	1 200
SN 2009ip	2012-Sep-22	R3000	1 200
SN 2009ip	2012-Sep-23	B3000	1 200
SN 2009ip	2012-Sep-23	R3000	1 200
SN 2009ip	2013-Apr-12	B7000	1 200
SN 2009ip	2013-Apr-12	R7000	1 200
SN 2009ip	2013-Jun-22	B7000	1 200
SN 2009ip	2013-Jun-22	R7000	1 200
SN 2009ip	2013-May-26	B3000	1 200
SN 2009ip	2013-May-26	R7000	1 200
SN 2012ca	2012-Aug-10	B3000	1 200
SN 2012ca	2012-Aug-10	R3000	1 200
SN 2012ca	2012-Sep-06	B3000	1 200
SN 2012ca	2012-Sep-06	R3000	1 200
SN 2012ca	2012-Sep-07	B3000	1 200
SN 2012ca	2012-Sep-07	R3000	1 200
SN 2012ca	2012-Sep-22	B3000	1 200
SN 2012ca	2012-Sep-22	R3000	1 200
SN 2012ca	2012-Sep-23	B3000	1 200
SN 2012ca	2012-Sep-23	R3000	1 200
SN 2012ca	2013-Jun-03	B3000	1 200
SN 2012ca	2013-Jun-03	R7000	1 200
SN 2012ca	2013-May-26	B3000	1 200
SN 2012ca	2013-May-26	R3000	1 200
SN 2012ca	2013-May-26	R7000	1 200
SN 2012dj	2012-Aug-11	B3000	1 200
SN 2012dj	2012-Aug-11	R3000	1 200
SN 2012dj	2012-Aug-12	B3000	1 200
SN 2012dj	2012-Aug-12	R3000	1 200
SN 2012dj	2012-Aug-13	B3000	1 200
SN 2012dj	2012-Aug-13	R3000	1 200
SN 2012dj	2012-Sep-06	B3000	1 200
SN 2012dj	2012-Sep-06	R3000	1 200
SN 2012dj	2012-Sep-07	B3000	1 200
SN 2012dj	2012-Sep-07	R3000	1 200
SN 2012dj	2012-Sep-22	B3000	1 200
SN 2012dj	2012-Sep-22	R3000	1 200
SN 2012dj	2012-Sep-23	B3000	1 200
SN 2012dj	2012-Sep-23	R3000	1 200
SN 2012dn	2012-Aug-11	B3000	1 200
SN 2012dn	2012-Aug-11	R3000	1 200
SN 2012dn	2012-Aug-12	B3000	1 200
SN 2012dn	2012-Aug-12	R3000	1 200
SN 2012dn	2012-Aug-13	B3000	1 200
SN 2012dn	2012-Aug-13	R3000	1 200
SN 2012dn	2012-Jul-18	B3000	600
SN 2012dn	2012-Jul-18	R3000	600
SN 2012dn	2012-Jul-19	B3000	600
SN 2012dn	2012-Jul-19	R3000	600
SN 2012dn	2012-Jul-20	B3000	180
SN 2012dn	2012-Jul-20	R3000	180
SN 2012dn	2012-Jul-21	B3000	1 200
SN 2012dn	2012-Jul-21	R3000	1 200
SN 2012dn	2012-Oct-23	B3000	1 200
SN 2012dn	2012-Oct-23	R3000	1 200
SN 2012dn	2012-Sep-06	B3000	1 200
SN 2012dn	2012-Sep-06	R3000	1 200

Table A3. Continued.

SN	Observation date	Grating	Exposure time (s)
SN 2012dn	2012-Sep-07	B3000	1 200
SN 2012dn	2012-Sep-07	R3000	1 200
SN 2012dn	2012-Sep-22	B3000	1 200
SN 2012dn	2012-Sep-22	R3000	1 200
SN 2012dn	2012-Sep-23	B3000	1 200
SN 2012dn	2012-Sep-23	R3000	1 200
SN 2012dt	2012-Sep-22	B3000	1 200
SN 2012dt	2012-Sep-22	R3000	1 200
SN 2012dy	2012-Aug-11	B3000	1 200
SN 2012dy	2012-Aug-11	R3000	1 200
SN 2012dy	2012-Aug-12	B3000	1 200
SN 2012dy	2012-Aug-12	R3000	1 200
SN 2012dy	2012-Aug-13	B3000	1 200
SN 2012dy	2012-Aug-13	R3000	1 200
SN 2012dy	2012-Sep-06	B3000	1 200
SN 2012dy	2012-Sep-06	R3000	1 200
SN 2012dy	2012-Sep-07	B3000	1 200
SN 2012dy	2012-Sep-07	R3000	1 200
SN 2012dy	2012-Sep-22	B3000	1 200
SN 2012dy	2012-Sep-22	R3000	1 200
SN 2012dy	2012-Sep-23	B3000	1 200
SN 2012dy	2012-Sep-23	R3000	1 200
SN 2012ec	2012-Aug-12	B3000	1 200
SN 2012ec	2012-Aug-12	R3000	1 200
SN 2012ec	2012-Aug-13	B3000	1 200
SN 2012ec	2012-Aug-13	R3000	1 200
SN 2012ec	2012-Oct-22	B3000	1 200
SN 2012ec	2012-Oct-22	R3000	1 200
SN 2012ec	2012-Sep-01	B3000	600
SN 2012ec	2012-Sep-01	R3000	600
SN 2012ec	2012-Sep-03	B3000	700
SN 2012ec	2012-Sep-03	R3000	700
SN 2012ec	2012-Sep-06	B3000	1 200
SN 2012ec	2012-Sep-06	R3000	1 200
SN 2012ec	2012-Sep-07	B3000	1 200
SN 2012ec	2012-Sep-07	R3000	1 200
SN 2012ec	2012-Sep-22	B3000	1 200
SN 2012ec	2012-Sep-22	R3000	1 200
SN 2012ec	2012-Sep-23	B3000	1 200
SN 2012ec	2012-Sep-23	R3000	1 200
SN 2012eq	2012-Sep-07	B3000	1 200
SN 2012eq	2012-Sep-07	R3000	1 200
SN 2012eu	2012-Sep-07	B3000	1 200
SN 2012eu	2012-Sep-07	R3000	1 200
SN 2012hr	2013-Dec-30	B3000	1 200
SN 2012hr	2013-Dec-30	R3000	1 200
SN 2013K	2013-May-26	B3000	1 200
SN 2013K	2013-May-26	R3000	1 200
SN 2013aa	2013-Apr-09	B3000	1 200
SN 2013aa	2013-Apr-09	R3000	1 200
SN 2013aa	2013-Mar-25	B3000	1 200
SN 2013aa	2013-Mar-25	R3000	1 200
SN 2013aa	2013-Sep-13	B3000	1 200
SN 2013aa	2013-Sep-13	R3000	1 200
SN 2013aa	2014-Jan-31	B3000	1 200
SN 2013aa	2014-Jan-31	R3000	1 200
SN 2013ai	2013-Apr-09	B3000	1 200
SN 2013ai	2013-Apr-09	R3000	1 200
SN 2013ai	2013-Mar-08	B3000	1 200
SN 2013ai	2013-Mar-08	R3000	1 200
SN 2013ai	2013-Mar-25	B3000	1 200

Table A3. Continued.

SN	Observation date	Grating	Exposure time (s)
SN 2013ai	2013-Mar-25	R3000	1 200
SN 2013ai	2013-May-26	B3000	1 200
SN 2013ai	2013-May-26	R3000	1 200
SN 2013aj	2013-Mar-08	B3000	1 200
SN 2013aj	2013-Mar-08	R3000	1 200
SN 2013aj	2013-Mar-25	B3000	1 200
SN 2013aj	2013-Mar-25	R3000	1 200
SN 2013am	2013-Apr-09	B3000	1 200
SN 2013am	2013-Apr-09	R3000	1 200
SN 2013am	2013-Mar-24	B3000	1 200
SN 2013am	2013-Mar-24	B3000	1 800
SN 2013am	2013-Mar-24	R3000	1 200
SN 2013am	2013-Mar-24	R3000	1 800
SN 2013am	2013-Mar-25	B3000	1 200
SN 2013am	2013-Mar-25	R3000	1 200
SN 2013am	2013-Mar-27	B3000	1 500
SN 2013am	2013-Mar-27	R3000	1 500
SN 2013ao	2013-Mar-25	B3000	1 200
SN 2013ao	2013-Mar-25	R3000	1 200
SN 2013bj	2013-Apr-12	B3000	1 200
SN 2013bj	2013-Apr-12	R3000	1 200
SN 2013bk	2013-Apr-12	B3000	1 200
SN 2013bk	2013-Apr-12	R3000	1 200
SN 2013by	2013-Aug-19	B3000	1 200
SN 2013by	2013-Aug-19	R3000	1 200
SN 2013by	2013-May-26	B3000	1 200
SN 2013by	2013-May-26	R3000	1 200
SN 2013by	2014-Jul-08	B3000	1 200
SN 2013by	2014-Jul-08	R3000	1 200
SN 2013bz	2013-May-26	B3000	1 200
SN 2013bz	2013-May-26	R3000	1 200
SN 2013cg	2013-May-26	B3000	1 200
SN 2013cg	2013-May-26	R3000	1 200
SN 2013cg	2013-May-26	R7000	1 200
SN 2013cs	2013-May-26	B3000	1 200
SN 2013cs	2013-May-26	R3000	1 200
SN 2013cs	2013-May-26	R7000	1 200
SN 2013cs	2014-Mar-22	B3000	1 200
SN 2013cs	2014-Mar-22	R3000	1 200
SN 2013cy	2013-Jun-03	B3000	1 200
SN 2013cy	2013-Jun-03	R3000	1 200
SN 2013cz	2013-Jun-03	B3000	1 200
SN 2013cz	2013-Jun-03	R3000	1 200
SN 2013df	2013-Jun-22	B3000	1 200
SN 2013df	2013-Jun-22	R3000	1 200
SN 2013dh	2013-Jul-01	B3000	1 800
SN 2013dh	2013-Jul-01	R3000	1 800
SN 2013dh	2013-Jun-22	B3000	1 200
SN 2013dh	2013-Jun-22	R3000	1 200
SN 2013du	2013-Jul-04	B3000	1 200
SN 2013du	2013-Jul-04	R3000	1 200
SN 2013ef	2013-Jul-04	B3000	1 200
SN 2013ef	2013-Jul-04	R3000	1 200
SN 2013ej	2013-Aug-11	B3000	1 200
SN 2013ej	2013-Aug-11	R3000	1 200
SN 2013ej	2013-Aug-19	B3000	1 200
SN 2013ej	2013-Aug-19	R3000	1 200
SN 2013ej	2013-Jul-31	B3000	1 200
SN 2013ej	2013-Jul-31	R3000	1 200
SN 2013ej	2013-Oct-16	B3000	1 200
SN 2013ej	2013-Oct-16	R3000	1 200

Table A3. Continued.

SN	Observation date	Grating	Exposure time (s)
SN 2013ej	2013-Oct-24	B3000	1 200
SN 2013ej	2013-Oct-24	R3000	1 200
SN 2013ej	2013-Sep-19	B3000	1 200
SN 2013ej	2013-Sep-19	R3000	1 200
SN 2013ek	2013-Aug-11	B3000	1 200
SN 2013ek	2013-Aug-11	R3000	1 200
SN 2013ek	2013-Aug-19	B3000	1 200
SN 2013ek	2013-Aug-19	R3000	1 200
SN 2013ek	2013-Jul-31	B3000	1 200
SN 2013ek	2013-Jul-31	R3000	1 200
SN 2013ek	2013-Sep-13	B3000	1 200
SN 2013ek	2013-Sep-13	R3000	1 200
SN 2013er	2013-Jul-31	B3000	1 200
SN 2013er	2013-Jul-31	R3000	1 200
SN 2013fd	2013-Sep-19	B3000	1 200
SN 2013fd	2013-Sep-19	R3000	1 200
SN 2013fj	2013-Sep-19	B3000	1 200
SN 2013fj	2013-Sep-19	R3000	1 200
SN 2013fq	2013-Oct-24	B3000	1 200
SN 2013fq	2013-Oct-24	R3000	1 200
SN 2013fq	2013-Sep-19	B3000	1 200
SN 2013fq	2013-Sep-19	R3000	1 200
SN 2013fs	2013-Nov-14	B3000	1 200
SN 2013fs	2013-Nov-14	R3000	1 200
SN 2013fs	2013-Nov-28	B3000	1 200
SN 2013fs	2013-Nov-28	R3000	1 200
SN 2013fs	2013-Oct-08	B3000	1 200
SN 2013fs	2013-Oct-08	R3000	1 200
SN 2013fs	2013-Oct-24	B3000	1 200
SN 2013fs	2013-Oct-24	R3000	1 200
SN 2013ft	2013-Oct-08	B3000	1 200
SN 2013ft	2013-Oct-08	R3000	1 200
SN 2013fw	2013-Nov-14	B3000	1 200
SN 2013fw	2013-Nov-14	R3000	1 200
SN 2013gh	2013-Aug-19	B3000	1 200
SN 2013gh	2013-Aug-19	R7000	1 200
SN 2013gh	2013-Aug-30	B3000	1 200
SN 2013gh	2013-Aug-30	R3000	1 200
SN 2013gh	2013-Aug-30	R7000	1 200
SN 2013gi	2013-Nov-14	B3000	1 200
SN 2013gi	2013-Nov-14	R3000	1 200
SN 2013gq	2013-Oct-08	B3000	1 200
SN 2013gq	2013-Oct-08	R3000	1 200
SN 2013gr	2013-Dec-06	B3000	1 200
SN 2013gr	2013-Dec-06	R3000	1 200
SN 2013gr	2013-Dec-15	B3000	1 200
SN 2013gr	2013-Dec-15	R3000	1 200
SN 2013gr	2013-Dec-19	B3000	1 200
SN 2013gr	2013-Dec-19	R3000	1 200
SN 2013gr	2013-Dec-29	B3000	1 200
SN 2013gr	2013-Dec-29	R3000	1 200
SN 2013gr	2014-Jan-18	B3000	1 200
SN 2013gr	2014-Jan-18	R3000	1 200
SN 2013hh	2013-Dec-12	B3000	1 200
SN 2013hh	2013-Dec-12	R3000	1 200
SN 2013hj	2013-Dec-19	B3000	1 200
SN 2013hj	2013-Dec-19	R3000	1 200
SN 2013hj	2013-Dec-29	B3000	1 200
SN 2013hj	2013-Dec-29	R3000	1 200
SN 2013hn	2013-Dec-19	B3000	1 200
SN 2013hn	2013-Dec-19	R3000	1 200

Table A3. Continued.

SN	Observation date	Grating	Exposure time (s)
SN 2013hn	2013-Dec-29	B3000	1 200
SN 2013hn	2013-Dec-29	R3000	1 200
SN 2013hn	2013-Jun-22	B3000	1 200
SN 2013hn	2013-Jun-22	R3000	1 200
SN 2013hu	2013-Dec-29	B3000	1 200
SN 2013hu	2013-Dec-29	R3000	1 200
SN 2013hx	2014-Feb-24	B3000	1 200
SN 2013hx	2014-Feb-24	R3000	1 200
SN 2013hx	2014-Jan-31	B3000	1 200
SN 2013hx	2014-Jan-31	R3000	1 200
SN 2013hx	2014-Mar-04	B3000	1 200
SN 2013hx	2014-Mar-04	R3000	1 200
SN 2013hx	2014-Mar-14	B3000	1 200
SN 2013hx	2014-Mar-14	R3000	1 200
SN 2014D	2014-Jan-18	B3000	1 200
SN 2014D	2014-Jan-18	R3000	1 200
SN 2014E	2014-Jan-18	B3000	1 200
SN 2014E	2014-Jan-18	R3000	1 200
SN 2014I	2014-Jan-18	B3000	1 200
SN 2014I	2014-Jan-18	R3000	1 200
SN 2014L	2014-Feb-24	B3000	1 200
SN 2014L	2014-Feb-24	R3000	1 200
SN 2014L	2014-Jan-31	B3000	1 200
SN 2014L	2014-Jan-31	R3000	1 200
SN 2014L	2014-Mar-14	B3000	1 200
SN 2014L	2014-Mar-14	R3000	1 200
SN 2014L	2014-Mar-22	B3000	1 200
SN 2014L	2014-Mar-22	R3000	1 200
SN 2014N	2014-Jan-31	B3000	1 200
SN 2014N	2014-Jan-31	R3000	1 200
SN 2014X	2014-Mar-04	B3000	1 200
SN 2014X	2014-Mar-04	R3000	1 200
SN 2014aa	2014-Apr-02	B3000	1 200
SN 2014aa	2014-Apr-02	R3000	1 200
SN 2014aa	2014-Mar-14	B3000	1 200
SN 2014aa	2014-Mar-14	R3000	1 200
SN 2014aa	2014-Mar-22	B3000	1 200
SN 2014aa	2014-Mar-22	R3000	1 200
SN 2014ac	2014-Mar-14	B3000	1 200
SN 2014ac	2014-Mar-14	R3000	1 200
SN 2014ad	2014-Apr-02	B3000	1 200
SN 2014ad	2014-Apr-02	R3000	1 200
SN 2014ad	2014-Apr-16	B3000	1 800
SN 2014ad	2014-Apr-16	R3000	1 800
SN 2014ad	2014-Apr-23	B3000	1 200
SN 2014ad	2014-Apr-23	R3000	1 200
SN 2014ad	2014-Mar-14	B3000	1 200
SN 2014ad	2014-Mar-14	R3000	1 200
SN 2014ad	2014-Mar-17	B3000	1 800
SN 2014ad	2014-Mar-17	R3000	1 800
SN 2014ad	2014-Mar-18	B3000	1 800
SN 2014ad	2014-Mar-18	R3000	1 800
SN 2014ad	2014-Mar-19	B3000	1 800
SN 2014ad	2014-Mar-19	R3000	1 800
SN 2014ad	2014-Mar-22	B3000	1 200
SN 2014ad	2014-Mar-22	R3000	1 200
SN 2014ad	2014-Mar-28	B3000	1000
SN 2014ad	2014-Mar-28	R3000	1000
SN 2014ah	2014-Apr-02	B3000	1 200
SN 2014ah	2014-Apr-02	R3000	1 200
SN 2014ao	2014-Apr-23	B3000	1 200
SN 2014ao	2014-Apr-23	R3000	1 200
SN 2014ao	2014-Apr-23	R7000	1 200
SN 2014ap	2014-Mar-22	B3000	1 200
SN 2014ap	2014-Mar-22	R3000	1 200
SN 2014at	2014-Apr-23	B3000	1 200
SN 2014at	2014-Apr-23	R3000	1 200
SN 2014at	2014-Apr-23	R7000	1 200
SN 2014au	2014-Apr-23	B3000	1 200
SN 2014au	2014-Apr-23	R3000	1 200
SN 2014bx	2014-Jul-22	B3000	200
SN 2014bx	2014-Jul-22	R3000	200
SN 2014bz	2014-Jun-11	B3000	800
SN 2014bz	2014-Jun-11	R3000	800
SN 2014ca	2014-Jun-11	B3000	800
SN 2014ca	2014-Jun-11	R3000	800
SN 2014cm	2014-Jun-11	B3000	800
SN 2014cm	2014-Jun-11	R3000	800
SN 2014co	2014-Jul-08	B3000	1 200
SN 2014co	2014-Jul-08	R3000	1 200
SN 2014cp	2014-Aug-05	B3000	1 200
SN 2014cp	2014-Aug-05	R3000	1 200
SN 2014cp	2014-Jul-08	B3000	1 200
SN 2014cp	2014-Jul-08	R3000	1 200
SN 2014cq	2014-Jul-08	B3000	1 200
SN 2014cq	2014-Jul-08	R3000	1 200
SN 2014cr	2014-Aug-05	B3000	1 200
SN 2014cr	2014-Aug-05	R3000	1 200
SN 2014cr	2014-Jul-08	B3000	1 200
SN 2014cr	2014-Jul-08	R3000	1 200
SN 2014cs	2014-Jul-08	B3000	1 200
SN 2014cs	2014-Jul-08	R3000	1 200
SN 2014ct	2014-Jun-12	B3000	800
SN 2014ct	2014-Jun-12	R3000	800
SN 2014cu	2014-Jul-08	B3000	1 200
SN 2014cu	2014-Jul-08	R3000	1 200
SN 2014cw	2014-Sep-09	B3000	1 200
SN 2014cw	2014-Sep-09	R3000	1 200
SN 2014cx	2014-Sep-09	B3000	1 200
SN 2014cx	2014-Sep-09	R3000	1 200
SN 2014cx	2014-Sep-10	B3000	1 200
SN 2014cx	2014-Sep-10	R3000	1 200
SN 2014cy	2014-Sep-09	B3000	1 200
SN 2014cy	2014-Sep-09	R3000	1 200
SN 2014dc	2014-Sep-10	B3000	1 200
SN 2014dc	2014-Sep-10	R3000	1 200
SN 2014df	2014-Jun-04	B3000	900
SN 2014df	2014-Jun-04	R3000	900
SN 2014dl	2014-Oct-03	B3000	1 200
SN 2014dl	2014-Oct-03	R3000	1 200
SN 2014dn	2014-Oct-03	B3000	1 200
SN 2014dn	2014-Oct-03	R3000	1 200
SN 2014dn	2014-Oct-09	B3000	1 200
SN 2014dn	2014-Oct-09	R3000	1 200
SN 2014do	2014-Oct-03	B3000	1 200
SN 2014do	2014-Oct-03	R3000	1 200
SN 2014dp	2014-Oct-09	B3000	1 200
SN 2014dp	2014-Oct-09	R3000	1 200
SN 2014dq	2014-Nov-14	B3000	1 200
SN 2014dq	2014-Nov-14	R3000	1 200
SN 2014dq	2014-Oct-27	B3000	1 200
SN 2014dq	2014-Oct-27	R3000	1 200

Table A3. Continued.

SN	Observation date	Grating	Exposure time (s)
SN 2014dr	2014-Oct-18	B3000	1 200
SN 2014dr	2014-Oct-18	R3000	1 200
SN 2014eg	2015-Jan-29	B3000	1 200
SN 2014eg	2015-Jan-29	R7000	1 200
SN 2014eg	2015-Mar-05	B3000	1 200
SN 2014eg	2015-Mar-05	R3000	1 200
SN 2015F	2015-Apr-11	B3000	1 200
SN 2015F	2015-Apr-11	R3000	1 200
SN 2015F	2015-Apr-29	B3000	1 200
SN 2015F	2015-Apr-29	R3000	1 200
SN 2015F	2015-Jul-08	B3000	1 200
SN 2015F	2015-Jul-08	R3000	1 200
SN 2015F	2015-Mar-12	B3000	1 200
SN 2015F	2015-Mar-12	R3000	1 200
SN 2015J	2015-Aug-17	B3000	1 200
SN 2015J	2015-Aug-17	R7000	1 200
SN 2015J	2015-Jul-01	B3000	1 200
SN 2015J	2015-Jul-01	R7000	1 200
SN 2015J	2015-Jul-08	B3000	1 200
SN 2015J	2015-Jul-08	R7000	1 200
SN 2015J	2015-Jul-25	B3000	900
SN 2015J	2015-Jul-25	R3000	900
SN 2015J	2015-Jul-31	B3000	1 200
SN 2015J	2015-Jul-31	R3000	1 200
SN 2015J	2015-Jun-24	B3000	1 200
SN 2015J	2015-Jun-24	R3000	1 200
ASASSN-13co	2013-Sep-19	B3000	1 200
ASASSN-13co	2013-Sep-19	R3000	1 200
ASASSN-14dp	2014-Jul-08	B3000	1 200
ASASSN-14dp	2014-Jul-08	R3000	1 200
ASASSN-14eu	2014-Aug-05	B3000	1 200
ASASSN-14eu	2014-Aug-05	R3000	1 200
ASASSN-14ew	2014-Sep-10	B3000	1 200
ASASSN-14ew	2014-Sep-10	R3000	1 200
ASASSN-14fo	2014-Sep-10	B3000	1 200
ASASSN-14fo	2014-Sep-10	R3000	1 200
ASASSN-14fw	2014-Sep-10	B3000	1 200
ASASSN-14fw	2014-Sep-10	R3000	1 200
ASASSN-14gs	2014-Sep-09	B3000	1 200
ASASSN-14gs	2014-Sep-09	R3000	1 200
ASASSN-14ha	2014-Nov-06	B3000	1 200
ASASSN-14ha	2014-Nov-06	R3000	1 200
ASASSN-14ha	2014-Oct-03	B3000	1 200
ASASSN-14ha	2014-Oct-03	R3000	1 200
ASASSN-14ha	2014-Oct-09	B3000	1 200
ASASSN-14ha	2014-Oct-09	R3000	1 200
ASASSN-14ha	2014-Oct-18	B3000	1 200
ASASSN-14ha	2014-Oct-18	R3000	1 200
ASASSN-14ha	2014-Oct-27	B3000	1 200
ASASSN-14ha	2014-Oct-27	R3000	1 200
ASASSN-14hr	2014-Oct-03	B3000	1 200
ASASSN-14hr	2014-Oct-03	R3000	1 200
ASASSN-14hu	2014-Nov-06	B3000	1 200
ASASSN-14hu	2014-Nov-06	R3000	1 200
ASASSN-14hu	2014-Oct-03	B3000	1 200
ASASSN-14hu	2014-Oct-03	R3000	1 200
ASASSN-14hu	2014-Oct-09	B3000	1 200
ASASSN-14hu	2014-Oct-09	R3000	1 200
ASASSN-14hu	2014-Oct-18	B3000	1 200
ASASSN-14hu	2014-Oct-18	R3000	1 200
ASASSN-14hu	2014-Oct-27	B3000	1 200

Table A3. Continued.

SN	Observation date	Grating	Exposure time (s)
ASASSN-14hu	2014-Oct-27	R3000	1 200
ASASSN-14ig	2014-Oct-03	B3000	1 200
ASASSN-14ig	2014-Oct-03	R3000	1 200
ASASSN-14ih	2014-Oct-03	B3000	1 200
ASASSN-14ih	2014-Oct-03	R3000	1 200
ASASSN-14ii	2014-Oct-03	B3000	1 200
ASASSN-14ii	2014-Oct-03	R3000	1 200
ASASSN-14il	2014-Oct-03	B3000	1 200
ASASSN-14il	2014-Oct-03	R3000	1 200
ASASSN-14il	2014-Oct-09	B3000	1 200
ASASSN-14il	2014-Oct-09	R3000	1 200
ASASSN-14il	2014-Oct-18	B3000	1 200
ASASSN-14il	2014-Oct-18	R3000	1 200
ASASSN-14il	2014-Oct-27	B3000	1 200
ASASSN-14il	2014-Oct-27	R3000	1 200
ASASSN-14jc	2014-Nov-06	B3000	1 200
ASASSN-14jc	2014-Nov-06	R3000	1 200
ASASSN-14jc	2014-Oct-27	B3000	1 200
ASASSN-14jc	2014-Oct-27	R3000	1 200
ASASSN-14jg	2014-Nov-06	B3000	1 200
ASASSN-14jg	2014-Nov-06	R3000	1 200
ASASSN-14ko	2014-Dec-16	B3000	1 200
ASASSN-14ko	2014-Dec-16	R7000	1 200
ASASSN-14ko	2015-Feb-15	B3000	1 200
ASASSN-14ko	2015-Feb-15	R3000	1 200
ASASSN-14ko	2015-Jan-15	B3000	1 200
ASASSN-14ko	2015-Jan-15	R7000	1 200
ASASSN-14kp	2014-Nov-26	B3000	1 200
ASASSN-14kp	2014-Nov-26	R3000	1 200
ASASSN-14kq	2014-Nov-26	B3000	1 200
ASASSN-14kq	2014-Nov-26	R3000	1 200
ASASSN-14lp	2015-Apr-29	B3000	1 200
ASASSN-14lp	2015-Apr-29	R3000	1 200
ASASSN-14lp	2015-Jul-01	B3000	1 200
ASASSN-14lp	2015-Jul-01	R3000	1 200
ASASSN-14lt	2014-Dec-16	B3000	1 200
ASASSN-14lt	2014-Dec-16	R3000	1 200
ASASSN-14lw	2014-Dec-16	B3000	1 200
ASASSN-14lw	2014-Dec-16	R3000	1 200
ASASSN-14lw	2015-Feb-15	B3000	1 200
ASASSN-14lw	2015-Feb-15	R3000	1 200
ASASSN-14lw	2015-Jan-06	B3000	1 200
ASASSN-14lw	2015-Jan-06	R3000	1 200
ASASSN-14lw	2015-Jun-24	B3000	1 200
ASASSN-14lw	2015-Jun-24	R3000	1 200
ASASSN-15aj	2015-Feb-15	B3000	1 200
ASASSN-15aj	2015-Feb-15	R3000	1 200
ASASSN-15aj	2015-Feb-24	B3000	1 200
ASASSN-15aj	2015-Feb-24	R3000	1 200
ASASSN-15aj	2015-Mar-05	B3000	1 200
ASASSN-15aj	2015-Mar-05	R3000	1 200
ASASSN-15al	2015-Jan-15	B3000	1 200
ASASSN-15al	2015-Jan-15	R7000	1 200
ASASSN-15as	2015-Jan-16	B3000	1 200
ASASSN-15as	2015-Jan-16	R7000	1 200
ASASSN-15az	2015-Jan-16	B3000	1 200
ASASSN-15az	2015-Jan-16	R7000	1 200
ASASSN-15ba	2015-Feb-15	B3000	1 200
ASASSN-15ba	2015-Feb-15	R3000	1 200
ASASSN-15ba	2015-Feb-24	B3000	1 200
ASASSN-15ba	2015-Feb-24	R3000	1 200

Table A3. Continued.

SN	Observation date	Grating	Exposure time (s)
ASASSN-15ba	2015-Jan-25	B3000	1 200
ASASSN-15ba	2015-Jan-25	R3000	1 200
ASASSN-15ba	2015-Jan-29	B3000	1 200
ASASSN-15ba	2015-Jan-29	R3000	1 200
ASASSN-15ba	2015-Jul-08	B3000	1 200
ASASSN-15ba	2015-Jul-08	R3000	1 200
ASASSN-15ba	2015-Mar-12	B3000	1 200
ASASSN-15ba	2015-Mar-12	R3000	1 200
ASASSN-15dz	2015-Mar-05	B3000	1 200
ASASSN-15dz	2015-Mar-05	R3000	1 200
ASASSN-15eb	2015-Mar-05	B3000	1 200
ASASSN-15eb	2015-Mar-05	R3000	1 200
ASASSN-15ek	2015-Mar-12	B3000	1 200
ASASSN-15ek	2015-Mar-12	R3000	1 200
ASASSN-15go	2015-Apr-11	B3000	1 200
ASASSN-15go	2015-Apr-11	R3000	1 200
ASASSN-15hs	2015-Apr-29	B3000	1 200
ASASSN-15hs	2015-Apr-29	R3000	1 200
ASASSN-15hx	2015-Apr-29	B3000	1 200
ASASSN-15hx	2015-Apr-29	R3000	1 200
ASASSN-15hx	2015-Aug-17	B3000	600
ASASSN-15hx	2015-Aug-17	R3000	600
ASASSN-15hx	2015-Jul-08	B3000	1 200
ASASSN-15hx	2015-Jul-08	R3000	1 200
ASASSN-15hx	2015-Jul-31	B3000	1 200
ASASSN-15hx	2015-Jul-31	R3000	1 200
ASASSN-15hx	2015-Jun-24	B3000	1 200
ASASSN-15hx	2015-Jun-24	R3000	1 200
ASASSN-15hy	2015-Apr-29	B3000	1 200
ASASSN-15hy	2015-Apr-29	R3000	1 200
ASASSN-15hy	2015-Aug-17	B3000	1 200
ASASSN-15hy	2015-Aug-17	R3000	1 200
ASASSN-15hy	2015-Jul-01	B3000	1 200
ASASSN-15hy	2015-Jul-01	R3000	1 200
ASASSN-15hy	2015-Jul-08	B3000	1 200
ASASSN-15hy	2015-Jul-08	R3000	1 200
ASASSN-15hy	2015-Jul-31	B3000	1 200
ASASSN-15hy	2015-Jul-31	R3000	1 200
ASASSN-15hy	2015-Jun-24	B3000	1 200
ASASSN-15hy	2015-Jun-24	R3000	1 200
ASASSN-15hy	2015-May-03	B3000	900
ASASSN-15hy	2015-May-03	R3000	900
ASASSN-15hy	2015-May-07	B3000	1 200
ASASSN-15hy	2015-May-07	R3000	1 200
ASASSN-15hy	2015-May-13	B3000	600
ASASSN-15hy	2015-May-13	R3000	600
ASASSN-15hz	2015-Apr-29	B3000	1 200
ASASSN-15hz	2015-Apr-29	R3000	1 200
ASASSN-15ic	2015-Apr-29	B3000	1 200
ASASSN-15ic	2015-Apr-29	R3000	1 200
ASASSN-15lh	2015-Jul-01	B3000	1 200
ASASSN-15lh	2015-Jul-01	R3000	1 200
ASASSN-15lh	2015-Jul-08	B3000	1 200
ASASSN-15lh	2015-Jul-08	R3000	1 200
ASASSN-15lh	2015-Jul-31	B3000	1 200
ASASSN-15lh	2015-Jul-31	R3000	1 200
ASASSN-15lh	2015-Jun-24	B3000	1 200
ASASSN-15lh	2015-Jun-24	R3000	1 200
ASASSN-15lv	2015-Jul-01	B3000	1 200
ASASSN-15lv	2015-Jul-01	R3000	1 200
CSS1222	2014-Apr-02	B3000	1 200

Table A3. Continued.

SN	Observation date	Grating	Exposure time (s)
CSS1222	2014-Apr-02	R3000	1 200
Gaia15agm	2015-Jul-01	B3000	1 200
Gaia15agm	2015-Jul-01	R3000	1 200
LSQ12dlf	2012-Aug-11	B3000	1 200
LSQ12dlf	2012-Aug-11	R3000	1 200
LSQ12dlf	2012-Aug-12	B3000	1 200
LSQ12dlf	2012-Aug-12	R3000	1 200
LSQ12dlf	2012-Aug-13	B3000	1 200
LSQ12dlf	2012-Aug-13	R3000	1 200
LSQ12ege	2012-Aug-11	B3000	1 200
LSQ12ege	2012-Aug-11	R3000	1 200
LSQ12ege	2012-Aug-12	B3000	1 200
LSQ12ege	2012-Aug-12	R3000	1 200
LSQ12ege	2012-Aug-13	B3000	1 200
LSQ12ege	2012-Aug-13	R3000	1 200
LSQ12ehh	2012-Aug-11	B3000	1 200
LSQ12ehh	2012-Aug-11	R3000	1 200
LSQ12ehh	2012-Aug-12	B3000	1 200
LSQ12ehh	2012-Aug-12	R3000	1 200
LSQ12ehh	2012-Aug-13	B3000	1 200
LSQ12ehh	2012-Aug-13	R3000	1 200
LSQ12ers	2012-Sep-06	B3000	1 200
LSQ12ers	2012-Sep-06	R3000	1 200
LSQ12euu	2012-Sep-06	B3000	1 200
LSQ12euu	2012-Sep-06	R3000	1 200
LSQ12eve	2012-Sep-06	B3000	1 200
LSQ12eve	2012-Sep-06	R3000	1 200
LSQ12gdj	2012-Nov-19	B3000	1 200
LSQ12gdj	2012-Nov-19	R3000	1 200
LSQ12gdj	2012-Nov-20	B3000	1 200
LSQ12gdj	2012-Nov-20	R3000	1 200
LSQ12gdj	2012-Nov-21	B3000	1 200
LSQ12gdj	2012-Nov-21	R3000	1 200
LSQ13anm	2013-May-26	B3000	1 200
LSQ13anm	2013-May-26	R3000	1 200
LSQ13ddu	2013-Dec-06	B3000	1 200
LSQ13ddu	2013-Dec-06	R3000	1 200
LSQ13ddu	2013-Dec-15	B3000	1 200
LSQ13ddu	2013-Dec-15	R3000	1 200
LSQ13ddu	2013-Dec-19	B3000	1 200
LSQ13ddu	2013-Dec-19	R3000	1 200
LSQ13pp	2013-Mar-25	B3000	1 200
LSQ13pp	2013-Mar-25	R3000	1 200
LSQ14bcj	2014-Apr-23	B3000	1 200
LSQ14bcj	2014-Apr-23	R3000	1 200
LSQ14bcj	2014-Apr-23	R7000	1 200
LSQ15adm	2015-Apr-29	B3000	1 200
LSQ15adm	2015-Apr-29	R3000	1 200
LSQ15adm	2015-Aug-17	B3000	1 200
LSQ15adm	2015-Aug-17	R3000	1 200
LSQ15adm	2015-Jul-01	B3000	1 200
LSQ15adm	2015-Jul-01	R3000	1 200
LSQ15adm	2015-Jul-08	B3000	1 200
LSQ15adm	2015-Jul-08	R3000	1 200
LSQ15adm	2015-Jul-31	B3000	1 200
LSQ15adm	2015-Jul-31	R3000	1 200
LSQ15adm	2015-Jun-24	B3000	1 060
LSQ15adm	2015-Jun-24	R3000	1 060
LSQ15adm	2015-May-07	B3000	1 330
LSQ15adm	2015-May-07	R3000	1 330
LSQ15adm	2015-May-14	B3000	1 800

Table A3. Continued.

SN	Observation date	Grating	Exposure time (s)
LSQ15adm	2015-May-14	R3000	1 800
LSQ15ey	2015-Jan-29	B3000	1 200
LSQ15ey	2015-Jan-29	R3000	1 200
MASTERJ1408	2014-Apr-23	B3000	1 200
MASTERJ1408	2014-Apr-23	R7000	1 200
MASTERJ1353	2015-Mar-05	B3000	1 200
MASTERJ1353	2015-Mar-05	R3000	1 200
MASTERJ0746	2015-Apr-29	B3000	1 200
MASTERJ0746	2015-Apr-29	R3000	1 200
OGLE-2013-SN-070	2013-Oct-08	B3000	1 200
OGLE-2013-SN-070	2013-Oct-08	R3000	1 200
OGLE-2014-SN-019	2014-Feb-24	B3000	1 200
OGLE-2014-SN-019	2014-Feb-24	R3000	1 200
OGLE-2014-SN-019	2014-Mar-14	B3000	1 200
OGLE-2014-SN-019	2014-Mar-14	R3000	1 200
OGLE-2014-SN-021	2014-Feb-24	B3000	1 200
OGLE-2014-SN-021	2014-Feb-24	R3000	1 200
OGLE-2014-SN-021	2014-Mar-14	B3000	1 200
OGLE-2014-SN-021	2014-Mar-14	R3000	1 200
OGLE-2014-SN-067	2014-Aug-29	B3000	1 200
OGLE-2014-SN-067	2014-Aug-29	R3000	1 200
PS1-14lz	2014-Feb-24	B3000	1 200
PS1-14lz	2014-Feb-24	R3000	1 200
PS1-14md	2014-Feb-24	B3000	1 200
PS1-14md	2014-Feb-24	R3000	1 200
PS1-14ra	2014-Mar-14	B3000	1 200
PS1-14ra	2014-Mar-14	R3000	1 200
PS1-14vw	2014-Apr-02	B3000	1 200
PS1-14vw	2014-Apr-02	R3000	1 200
PS1-14vx	2014-Apr-02	B3000	1 200
PS1-14vx	2014-Apr-02	R3000	1 200
PS1-14wl	2014-Apr-02	B3000	1 200
PS1-14wl	2014-Apr-02	R3000	1 200
PS15ae	2015-Feb-24	B3000	1 200
PS15ae	2015-Feb-24	R3000	1 200
PS15ae	2015-Mar-12	B3000	1 200
PS15ae	2015-Mar-12	R3000	1 200
PS15br	2015-Mar-12	B3000	1 200
PS15br	2015-Mar-12	R3000	1 200
PSNJ02454138-0812301	2014-Oct-27	B3000	1 200
PSNJ02454138-0812301	2014-Oct-27	R3000	1 200
PSNJ05031639-0256110	2014-Nov-06	B3000	1 200
PSNJ05031639-0256110	2014-Nov-06	R3000	1 200
PSNJ09023787+2556042	2015-Apr-11	B3000	1 200
PSNJ09023787+2556042	2015-Apr-11	R3000	1 200
PSNJ09204691-0803340	2014-Dec-16	B3000	1 200
PSNJ09204691-0803340	2014-Dec-16	R7000	1 200
PSNJ09204691-0803340	2014-Nov-26	B3000	1 200
PSNJ09204691-0803340	2014-Nov-26	R3000	1 200
PSNJ09204691-0803340	2015-Feb-15	B3000	1 200
PSNJ09204691-0803340	2015-Feb-15	R3000	1 200
PSNJ09204691-0803340	2015-Jan-15	B3000	1 200
PSNJ09204691-0803340	2015-Jan-15	R7000	1 200
PSNJ09204691-0803340	2015-Jan-16	B3000	1 200
PSNJ09204691-0803340	2015-Jan-16	R7000	1 200
PSNJ10433393-3048206	2015-Feb-15	B3000	1 200
PSNJ10433393-3048206	2015-Feb-15	R3000	1 200
PSNJ11484578-2817312	2013-Dec-06	B3000	1 200
PSNJ11484578-2817312	2013-Dec-06	R3000	1 200
PSNJ13471211-2422171	2015-Feb-15	B3000	1 200
PSNJ13471211-2422171	2015-Feb-15	R3000	1 200

Table A3. Continued.

SN	Observation date	Grating	Exposure time (s)
PSNJ17194328-7721305	2013-Aug-30	B3000	1 200
PSNJ17194328-7721305	2013-Aug-30	R3000	1 200
PSNJ17194328-7721305	2013-Aug-30	R7000	1 200
PSNJ17194328-7721305	2014-Sep-09	B3000	1 200
PSNJ17194328-7721305	2014-Sep-09	R3000	1 200
PSNJ17285509-6609103	2013-Aug-30	B3000	1 200
PSNJ17285509-6609103	2013-Aug-30	R3000	1 200
PSNJ19251269-5336028	2015-Aug-17	B3000	1 200
PSNJ19251269-5336028	2015-Aug-17	R3000	1 200
PSNJ20250386-2449133	2014-Nov-06	B3000	1 200
PSNJ20250386-2449133	2014-Nov-06	R3000	1 200
PSNJ20250386-2449133	2014-Nov-14	B3000	1 200
PSNJ20250386-2449133	2014-Nov-14	R3000	1 200
PSNJ23320218-4545032	2012-Sep-07	B3000	1 200
PSNJ23320218-4545032	2012-Sep-07	R3000	1 200
PTF12gzk	2012-Aug-10	B3000	1 200
PTF12gzk	2012-Aug-10	R3000	1 200
PTF12gzk	2012-Aug-11	B3000	1 200
PTF12gzk	2012-Aug-11	R3000	1 200
PTF12gzk	2012-Aug-12	B3000	1 200
PTF12gzk	2012-Aug-12	R3000	1 200
PTF12gzk	2012-Aug-13	B3000	1 200
PTF12gzk	2012-Aug-13	R3000	1 200
PTF12gzk	2012-Sep-06	B3000	1 200
PTF12gzk	2012-Sep-06	R3000	1 200
PTF12gzk	2012-Sep-07	B3000	1 200
PTF12gzk	2012-Sep-07	R3000	1 200
PTF12gzk	2012-Sep-23	B3000	1 200
PTF12gzk	2012-Sep-23	R3000	1 200
iPTF13bvn	2013-Jun-22	B3000	1 200
iPTF13bvn	2013-Jun-22	R3000	1 200
iPTF13dge	2013-Dec-06	B3000	1 200
iPTF13dge	2013-Dec-06	R3000	1 200
iPTF13dge	2013-Oct-08	B3000	1 200
iPTF13dge	2013-Oct-08	R3000	1 200
iPTF13dge	2013-Oct-16	B3000	1 200
iPTF13dge	2013-Oct-16	R3000	1 200
iPTF13dge	2013-Sep-13	B3000	1 200
iPTF13dge	2013-Sep-13	R3000	1 200
iPTF13dge	2013-Sep-19	B3000	1 200
iPTF13dge	2013-Sep-19	R3000	1 200
iPTF13dge	2013-Sep-19	R7000	1 200
SMTJ10310056-3658262	2015-Apr-11	B3000	1 200
SMTJ10310056-3658262	2015-Apr-11	R3000	1 200
SMTJ03253351-5344190	2013-Dec-06	B3000	1 200
SMTJ03253351-5344190	2013-Dec-06	R3000	1 200
SMTJ05451320-4735425	2014-Jan-13	B3000	900
SMTJ05451320-4735425	2014-Jan-13	R3000	900
SMTJ13494831-0658174	2015-Aug-17	B3000	900
SMTJ13494831-0658174	2015-Aug-17	R7000	900
SNhunt222	2013-Dec-19	B3000	1 200
SNhunt222	2013-Dec-19	R3000	1 200
SNhunt239	2014-Apr-02	B3000	1 200
SNhunt239	2014-Apr-02	R3000	1 200
SNhunt259	2014-Oct-18	B3000	1 200
SNhunt259	2014-Oct-18	R3000	1 200
SNhunt261	2014-Oct-27	B3000	1 200
SNhunt261	2014-Oct-27	R3000	1 200

Table A4. Fits of Na line in SNe Ia.

SN	Observation datexs	Grating	v_{Na} (km s^{-1})	σ_{Na} (km s^{-1})	pEW_{Na} (Å)
ASASSN-14hr	2014-Oct-03	R3000	-41.3 ± 16.5	76.3 ± 13.6	0.74 ± 0.17
ASASSN-14jc	2014-Oct-27	R3000	-2.8 ± 11.5	65.3 ± 10.6	0.98 ± 0.19
ASASSN-14jg	2014-Nov-06	R3000	8.9 ± 15.3	58.1 ± 15.2	0.23 ± 0.07
ASASSN-15go	2015-Apr-11	R3000	82.9 ± 12.1	70.0 ± 10.6	1.75 ± 0.32
iPTF13dge	2013-Sep-19	R7000	-35.1 ± 3.3	22.3 ± 3.4	0.34 ± 0.05
LSQ14bcj	2014-Apr-23	R7000	20.9 ± 4.7	28.0 ± 4.9	0.99 ± 0.19
PS1-14wl	2014-Apr-02	R3000	35.9 ± 12.9	70.0 ± 0.0	1.22 ± 0.22
PSNJ13471211-2422171	2015-Feb-15	R3000	14.5 ± 49.6	119.4 ± 35.9	0.71 ± 0.26
PSNJ17194328-7721305	2013-Aug-30	R7000	-70.7 ± 3.2	24.3 ± 3.4	0.47 ± 0.07
SN 2012dn	2012-Jul-21	R3000	-9.4 ± 19.8	79.0 ± 17.2	0.25 ± 0.07
SN 2013aj	2013-Mar-08	R3000	5.0 ± 24.5	95.2 ± 18.8	0.43 ± 0.11
SN 2013cg	2013-May-26	R7000	42.0 ± 23.2	118.9 ± 16.6	1.39 ± 0.25
SN 2013cy	2013-Jun-03	R3000	45.2 ± 19.0	42.5 ± 20.8	0.19 ± 0.11
SN 2013er	2013-Jul-31	R3000	11.4 ± 16.3	78.4 ± 13.3	2.05 ± 0.44
SN 2013gh	2013-Aug-30	R7000	-18.9 ± 3.0	23.3 ± 3.1	1.50 ± 0.22
SN 2014aa	2014-Mar-14	R3000	-4.7 ± 43.5	130.0 ± 0.0	1.42 ± 0.34
SN 2014ao	2014-Apr-23	R7000	-7.2 ± 3.1	23.7 ± 3.2	1.33 ± 0.19
SN 2014at	2014-Apr-23	R3000	0.3 ± 41.8	130.0 ± 0.0	0.40 ± 0.14
SN 2014bx	2014-Jul-22	R3000	55.4 ± 12.9	73.7 ± 10.9	4.34 ± 0.79

Table A5. Host galaxy redshifts for SN Ia Na sample.

SN	Host	Redshift	Ref.[a]
ASASSN-14hr	2MASX J01504127-1431032	0.033620	6dF (Jones)
ASASSN-14jc	2MASX J07353554-6246099	0.011320	6dF (Jones)
ASASSN-14jg	PGC 128348	0.015315	Local
ASASSN-15go	(unknown)	0.019030	Local
iPTF13dge	NGC 1762	0.015854	(Theureau et al. 1998b)
LSQ14bcj	MCG -02-36-015	0.036056	Local
PS1-14wl	2MASX J13324055-2036204	0.032346	Local
PSNJ13471211-2422171	ESO 509-G108	0.019910	(Ogando et al. 2008)
PSNJ17194328-7721305	ESO 044-G010	0.009587	Local
SN 2012dn	ESO 462-G016	0.010187	(Theureau et al. 1998b)
SN 2013aj	NGC 5339	0.009126	(Theureau et al. 1998b)
SN 2013cg	NGC 2891	0.007952	(Ogando et al. 2008)
SN 2013cy	ESO 532-G025	0.031465	(da Costa et al. 1991)
SN 2013er	IC 850	0.018052	(Grogin, Geller, & Huchra 1998)
SN 2013gh	NGC 7183	0.009075	Local
SN 2014aa	NGC 3861	0.016982	(Cortese et al. 2008)
SN 2014ao	NGC 2615	0.014663	Local
SN 2014at	NGC 7119	0.032242	(Donzelli & Pastoriza 2000)
SN 2014bx	NGC 6808	0.011570	(Sandage & Tammann 1981)

[a] Via NED. 'Local' denotes local velocity measured with WiFeS, either from narrow lines in the SN spectrum or from galaxy rotation characteristics (see text for details).

a best fit relation of

$$\Delta m_{15} = 2.04 R_{Si} + 0.808. \qquad \text{(A1)}$$

The scatter about this best fit curve is 0.190 mag.